Heat transfer in a fluidized bed tubular solar receiver. On-sun experimental investigation

Ronny Gueguen, Guillaume Sahuquet, Michael Tessonneaud, Jean-Louis Sans, Emmanuel Guillot, Alex Le Gal, Roger Garcia, Samuel Mer, Adrien Toutant, Françoise Bataille, et al.

Solar Energy 265 (2023) 112118

Contents lists available at ScienceDirect

Solar Energy

journal homepage: www.elsevier.com/locate/solener

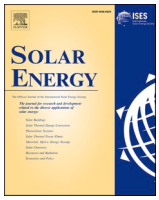

Heat transfer in a fluidized bed tubular solar receiver. On-sun experimental investigation

Ronny Gueguen [a], Guillaume Sahuquet [a], Michael Tessoneaud [a], Jean-Louis Sans [a], Emmanuel Guillot [a], Alex Le Gal [a], Roger Garcia [a], Samuel Mer [b], Adrien Toutant [b], Françoise Bataille [b], Gilles Flamant [a,*]

[a] Processes, Materials and Solar Energy Laboratory, PROMES-CNRS, 7 Rue du Four Solaire, 66120 Font-Romeu, France
[b] Processes, Materials and Solar Energy Laboratory, PROMES-CNRS, University of Perpignan (UPVD), Tecnosud, Rambla de la Thermodynamique, 66100 Perpignan, France

ARTICLE INFO

Keywords:
Tubular particle solar receiver
Particle-driven CSP
Geldart group A fluidized particles
Upward particle circulation
Heat transfer coefficient

ABSTRACT

Using particles as heat transfer fluid in a solar receiver is an attractive way to increase the global efficiency of solar power plants. In the case of the particle-in-tube solar receiver concept, the fluidized particles circulate vertically in tubes thanks to a controlled pressure gradient and an additional air injection. Experiments are conducted with olivine particles in a one-tube mock-up at the 1 MW CNRS solar furnace (France). The tube of high aspect ratio (more than 3 m height over 48 mm internal diameter) is irradiated along a 1-m height with several solar flux configurations that correspond to realistic operation conditions of a solar thermal power plant. The novelties of this paper lie in extending the operating parameters compared to earlier studies and in linking the fluidization regimes to wall heat transfer. Slugging, turbulent fluidization and fast fluidization regimes are detected within the receiver tube. It is shown that the system can tolerate high solar flux densities, up to 800 kW/m^2. The system proves to be highly controllable and flexible with respect to particle mass flux variation and transient operations. Particle temperature increase ranges from 100 to 650 °C depending on the particle mass flux. Maximum thermal efficiency and particle outlet temperature of respectively ~ 60 % and 680 °C are obtained, proving that this technology can be combined with highly efficient thermodynamic cycles. Global wall-to-particle heat transfer coefficient varies strongly with particle mass flux. It reaches a quasi-plateau above 15 kg/(m^{2}s) with a mean value of 1000 ± 200 W/(m^{2}K) and peaks data up to 1500 W/(m^{2}K). A dimensionless heat transfer index is derived to account for the effects of the particle mass flux on the experimental results. It highlights that both increasing the temperature and working in the turbulent fluidization regime result in the increase of the heat transfer between the tube walls and the particles.

1. Introduction

Concentrated solar power (CSP) plants produce electricity from direct solar irradiation. They offer the key advantage of being able to store the energy directly in the form of heat, in order to align electricity production and consumption. Current commercial power tower CSP plants use molten salt as heat transfer fluid (HTF) to absorb solar energy and store thermal energy, and a Rankine thermodynamic cycle to produce electricity. Increasing the overall efficiency of the power plants and reducing production cost are the shared objectives of the CSP community. The main option for the increase in efficiency of power tower is the integration of a high efficiency conversion cycle that operates at high temperature (>650 °C) while maintaining the main advantages of molten salt (both HTF and storage medium). An attractive solution for fulfilling the previous conditions is to use solid particles [18,34]. It offers the possibility to reach high solar receiver outlet temperatures – higher than 565 °C, which is the current limit with molten salt [11,50]. Temperature higher than 650 °C enables taking advantage of high efficiency thermodynamic cycles based on supercritical fluids (i.e. with water or CO_2) and reducing the total cost of the system [15]. In addition, unlike molten salt, particles do not freeze at low temperatures. Thus, it is no longer necessary to maintain a threshold temperature in the pipes – via electrical resistances – as in the case of molten salt. Consequently, the particle solution removes of the tracking electrical consumption. In addition, oxide particles are chemically stable, have a low toxicity, and

* Corresponding author.
E-mail address: Gilles.Flamant@promes.cnrs.fr (G. Flamant).

https://doi.org/10.1016/j.solener.2023.112118
Received 27 February 2023; Received in revised form 12 September 2023; Accepted 12 October 2023

Nomenclature

Abbreviations

CSP	Concentrated Solar Power
DNI	Direct Normal Irradiation
HTF	Heat Transfer Fluid
I.D.	Internal diameter

Arabic letters

$C_{p,part}$	Particle heat capacity (kJ/(kgK))
d_{sv}	Powder Sauter diameter (μm)
D_t	Tube internal diameter (m)
e_t	Tube thickness (mm)
g	Standard gravity (m/s^2)
G_p	Particle mass flux (kg/(m^{2}s))
H_t	Tube height (m)
$h_{wall,part}$	Wall-to-particle heat transfer coefficient (W/(m^{2}K))
$H_{wall,part}$	Dimensionless wall-to-particle heat transfer index (Ø)
$\dot{m}_p$	Particle mass flow rate (kg/s)
P_{tot}	Relative pressure in the dispenser (mbar)
$\dot{q_{ae}}$	Aeration flow rate (sm^3/h)
S_t	Internal tube section (m^2)
T_{disp}	Particle temperature in the dispenser (°C)
$T_{part,irr}$	Mean particle temperature in the irradiated zone of the tube (°C)
T^{out}_{part}	Particle temperature at the outlet of the irradiated zone of the tube (°C)
$T_{wall,int}$	Internal tube temperature (°C)
$T_{wall,ext}$	External tube temperature (°C)
U_{air}	Superficial air velocity (m/s)

Greek letters

α	Particle volume fraction (Ø)
α_{irr}	Mean particle volume fraction in the irradiated zone of the tube (Ø)
ΔT_{part}	Particle temperature increase in the solar receiver (°C)
$\Delta T_{wall,part}$	Logarithmic mean difference between the walls and particles temperatures (°C)
η_{th}	Thermal efficiency of the receiver (Ø)
ρ_{air}	Air density (kg/m^3)
ρ_{part}	Particle density (kg/m^3)
ϕ_{abs}	Absorbed power by the particles (kW)
φ_{sol}	Incident concentrated solar flux density (kW/m^2)
ϕ_{sol}	Incident concentrated solar power (kW)

low cost. The particle concept can be applied to medium power CSP plants [5].

Three main types of solar receiver using particles are currently being developed. First, the falling particle receiver, designed by Sandia National Laboratory – USA [31,32]. As suggested by its name, the particles are falling as a curtain and are directly irradiated by the concentrated solar flux. It enables working with high concentrated solar flux density (≥700 kW/m^2) associated to high efficiencies and temperatures, respectively around 6 70 % and 700 °C. However, several drawbacks appear as the loss of particles through the cavity aperture and the difficulty to control the particle flow rate, which is imposed by gravity. Second, the centrifugal receiver, designed by the German Aerospace Center – Germany [16,48]. The system is similar to a cement mixer (but working in the centrifugal mode), where the particle flow rate is controlled by the rotational speed of the receiver. The speed is adjusted depending on the incident solar flux. As for the falling particle receiver, the particles are directly irradiated. High receiver outlet temperatures (around 900 °C) have been obtained at lab-scale, which makes it a promising system. However, the receiver size is limited by the necessity to create a stable particle layer at the cylinder wall that limits its thermal power around few MW$_{th}$. Finally, the "particle-in-tube receiver", studied in this paper, developed by PROMES – CNRS laboratory in collaboration with European partners [12,42,17,19]. In this system, the particles are fluidized in a vessel, and circulate upward in vertical metallic irradiated tubes. The flow is imposed by both a pressure gradient and a secondary air injection. Particles are then indirectly heated by the hot internal surface of the tube. The air injection at the bottom of the receiver tubes stabilizes the particle mass flow and enables controlling the fluidization regimes of the suspension. Moreover, changing the injection air flow rate results in gradual variation of the particle mass flux in the tube. The main limitations associated with this concept are the energy used to fluidize the particles and the control of the fluidization regimes that considerably affect the wall-to-particles heat transfer and thus the thermal efficiency of the system [36,44]. Moreover, contrarily to the previously discussed concepts, the indirect heating of particles makes metal tube maximum operation temperature the main limiting factor. Nevertheless, the tubular receiver design is similar to commercial power tower receivers. It can therefore benefit from previous studies, especially concerning the design of a cavity-type receivers, aiming at limiting the thermal losses [20,26].

Table 1
Comparison between the on-sun experimental studies about the particle-in-tube concept of solar receiver.

Reference	[17]	[7]	[43]	[38]	*Present Study*
Particles	Silicon Carbide (SiC)	SiC	SiC	Olivine	Olivine
Particles Diameter (μm)	63.9	63.9	63.9	61	61
Internal Tube Diameter (mm)	36	36	29.7	46	48
Tube Height (m)	1	1	2.27	2.5	2.8
Irradiated Height (m)	0.5	0.5	1	1	1
Superficial Air Velocity (m/s)	0.011 – 0.109	0.021 – 0.042	0.09	0.03 – 0.11	0.025 – 0.469
Particle Mass Flux (kg/(m^{2}s))	7.4 – 24.6	10.2 – 45.1	17 – 44	20 – 110	0 – 93
Comments	One bare tube, proof of concept	One bare tube, extended parameters ranges	16 bare tubes inside a cavity	One finned tube	One bare tube

Since the 2010's, the particle-in-tube concept of solar receiver, also called "Upward Bubbling Fluidized Bed (UBFB)", has been studied in various configurations, gathered in Table 1. First, silicon carbide particles were used, mainly because of their thermal properties. After the proof of concept [17], experiments at ambient temperature were performed to understand the behavior of the gas-particle suspension [10], followed by simulations and on-sun experiments [7,6] with a 0.5 m irradiated tube. Then, a 150 kW$_{th}$ cavity solar receiver composed of 16 tubes, 1 m-height irradiated, has been built in the framework of the

Table 2
Properties of the olivine sample.

Sauter diameter d_{sv}	Bulk density ρ_{part}	Heat capacity $C_{p,part}$	Minimum Fluidization Velocity U_{mf}	Minimum Bubbling Velocity U_{mb}
61 μm	3300 kg/m^3	1 kJ/(kgK) if $T <$ 400 °C Eq.(1) if $T \geq$ 400 °C	0.42 cm/s	0.57 cm/s

CSP2 European project [43]. All these studies showed that this concept of solar receiver can operate with medium solar flux density on the tube walls – up to approximately 400 – 500 kW/m^2 – and led to particle temperatures increase (i.e. difference between the outlet and the inlet of the receiver) of approximately 500 °C. Then, cost and health properties of the particles have been taken into account in the framework of the Next CSP European project that led to the choice of olivine particles as solid material [35]. On-sun experiments have been performed with a single 1-m irradiated long finned tube. A global wall-to-particle heat transfer coefficient of roughly 1200 ± 400 W/(m^{2}K) was measured [38]. This result represents an intensification of the heat transfer compared to the previously cited studies. The main parameter responsible of this increase is the use of fins inside the tube that increases the transfer area. The particles size and physical properties have also a significant impact on the convective transfer. No experimental results with 1 m irradiated long bare tube have been reported. The other operating condition that influences the heat transfer is the fluidization regime. Previous works at ambient temperature identified the fluidization regimes in 3 m long tube [29,28]. They extended the ranges of the particle mass flux and the superficial air velocity compared to previous studies, determined the existence of several fluidization regimes within the tube and their transitions. The turbulent fluidization regime is theoretically associated to the best heat transfer rate [9,24], and it is thus the expected optimal regime for a fluidized particle solar receiver. Nevertheless, the effect of temperature on the regimes transitions velocities is not well known, justifying additional experimental campaign. More generally, the understanding of the suspension behavior at high temperature is necessary to define a control strategy of the solar receiver.

In this context, this paper aims at measuring and characterizing the thermal performances of a single particle-in-tube solar receiver tube using olivine particles as HTF over a large range of the operating

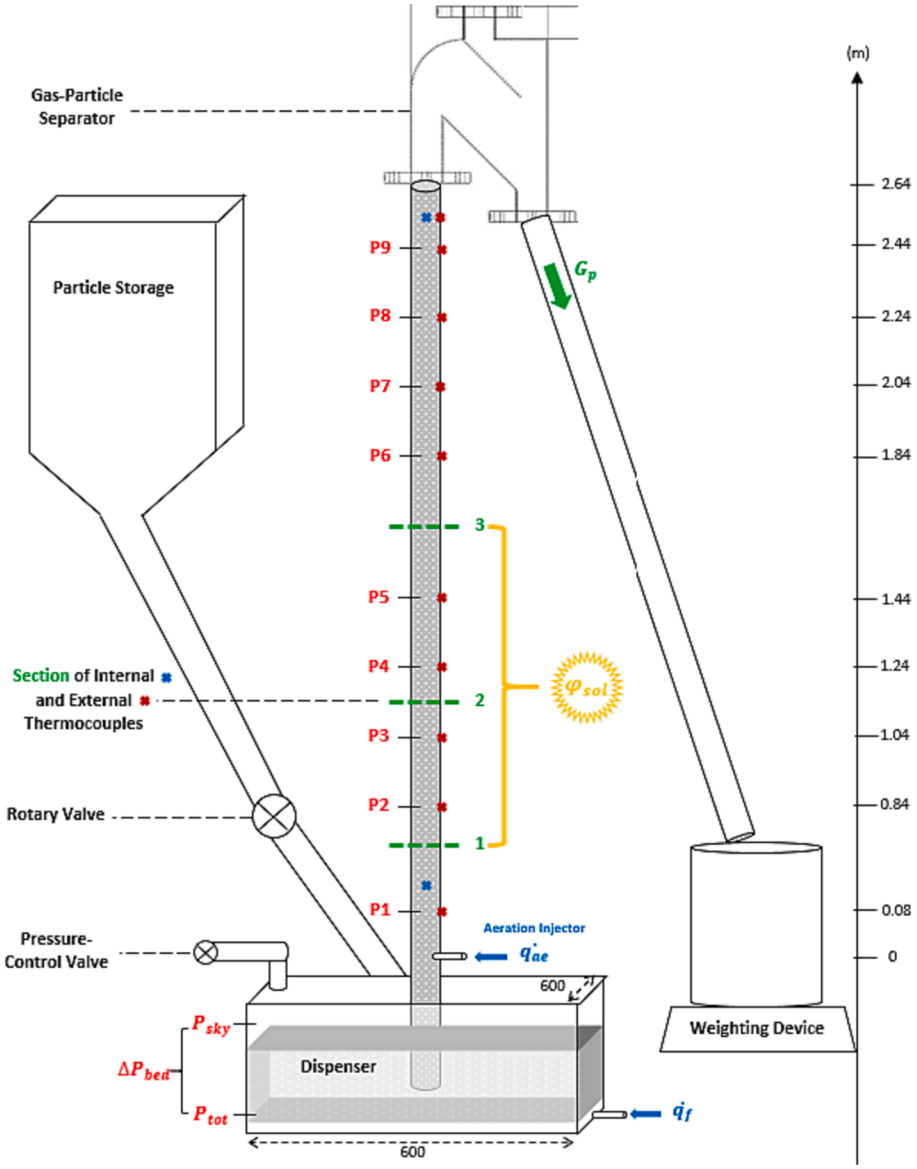

Fig. 1. Schematic representation of the receiver tube.

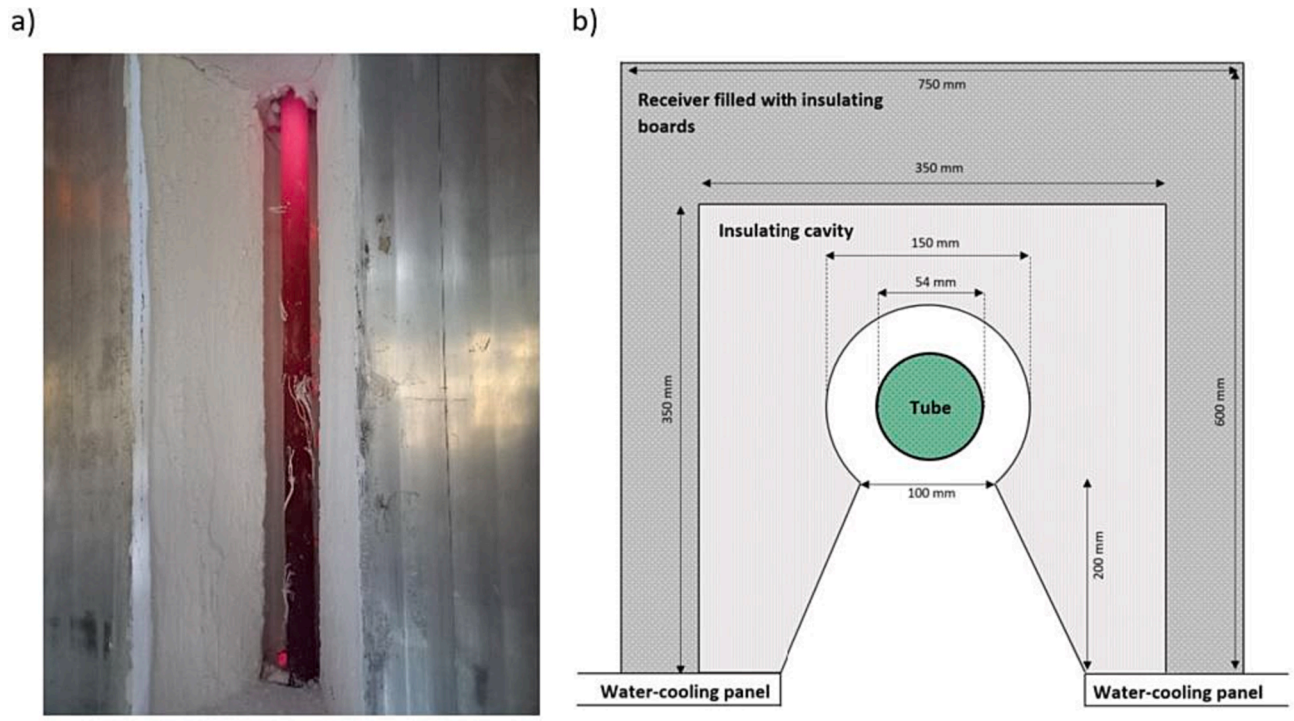

Fig. 2. a) picture of the receiver tube inside its cavity after an on-sun experiment, and b) schematic representation of the tube inside the cavity.

parameters. The behavior of such a solar receiver is first presented in terms of response to control parameters and transient regime. Then, the thermal performances are described. Finally, the wall-to-particle heat transfer coefficients are determined and correlated with the fluidization regimes.

2. Experimental Set-Up

2.1. Particles

Properties of olivine particles used are presented in Table 2. More details can be found in [29]. Both the Sauter diameter d_{sv} and the density ρ_{part} confirm that they belong to the group A of the Geldart classification [23]. Consequently, fluidization of such particles occurs at low air velocities. The heat capacity, $C_{p,part}$, is given by Equation (1) (with T the temperature in degree Celsius). For particle temperature below 400 °C, the heat capacity is fixed to 1 kJ/(kgK) [35,38].

The storage capacity of the suspension can be estimated by calculating the apparent volume heat capacity, given by $\alpha\rho_{part}C_{p,part}$. Assuming an average particle volume fraction α of 0.48 (measured for the fixed bed), this yields an apparent volume heat capacity of around 1.6 MJ/(m^{3}K). This value is in the same order of magnitude than the one of commonly used liquid HTFs [8]. While the storage capacity obtained is twice higher for molten salt, the price per ton of olivine is almost ten times lower (about \$100-\$150/ton [8,35]).

$$C_{p,part}(T) = 9.70{*}10^{-8}T^3 - 2.62{*}10^{-4}T^2 + 0.73T + 806 \quad (1)$$

2.2. Set-Up description

The experimental setup is illustrated in Fig. 1. The olivine particles are fluidized in a "dispenser" vessel – at the bottom of the mock-up – of squared section of 0.36 m^2, with an air flow rate of 10.6 sm^3/h. It corresponds to a fluidization velocity of 0.97 cm/s, i.e. 1.7 times the minimum bubbling velocity U_{mb}. This air flow passes through a sintered porous bronze plate distributor that enables a homogeneous freely bubbling fluidization regime inside the dispenser.

The receiver is composed of a single Inconel 601® tube of internal diameter (I.D.) $D_t = 48$ mm and thickness $e_t = 3$ mm. The bottom tip of the tube is plunged inside the dispenser fluidized bed. Increasing the pressure in the dispenser, thanks to a leak valve, results in an upward fluidized particle flow in the tube. The latter is driven by the pressure difference between the overpressure imposed in the dispenser P_{tot} and the atmospheric pressure at the top of the tube. The particles are indirectly heated thanks to concentrated solar radiation over a 1-m high zone, identified in yellow in the figure. The tube is painted with an absorbing black paint Pyromark® [1,33] to maximize the solar absorption. Furthermore, the tube is placed inside an insulating cavity with an aperture of 0.1-m width and 1-m height to reduce the thermal losses. The insulating material is painted with highly reflective white magnesium oxide. Fig. 2a shows a picture of the receiver tube inside its cavity after an experiment. A water-cooled panel is placed in front of the cavity that is filled with insulating boards – Insulfrax® insulating material [41], as shown in Fig. 2b.

A secondary air flow rate $\dot{q_{ae}}$, called "aeration", is injected at the bottom of the tube, 50 cm above the porous distributor in the dispenser, through a nozzle of 1.5 mm I.D.. It enables to both stabilize the gas-particle suspension [10] and control the fluidization regimes within the tube [29,28]. The aeration injection height is chosen as the reference height in this study, leading to a tube height $H_t = 2.80$ m. When the height of the suspension reaches this limit, the particles flow outside of the receiver in a tank placed on a weighing scale (see Fig. 1).

2.3. Instrumentation

Eleven pressure probes are implemented in the system (in red in Fig. 1). Two are placed in the dispenser, to measure both the total pressure P_{tot} and the pressure drop through the fluidized bed. The latter is directly related to the mass of particles and allows to keep it approximately constant during a test. Particles feed the dispenser from the storage tank thanks to a vane motor to maintain stationary conditions. Moreover, nine pressure probes are implemented along the tube, regularly spaced. The heights of the probes are detailed in Appendix A. They are connected to differential and relative pressure sensors, to

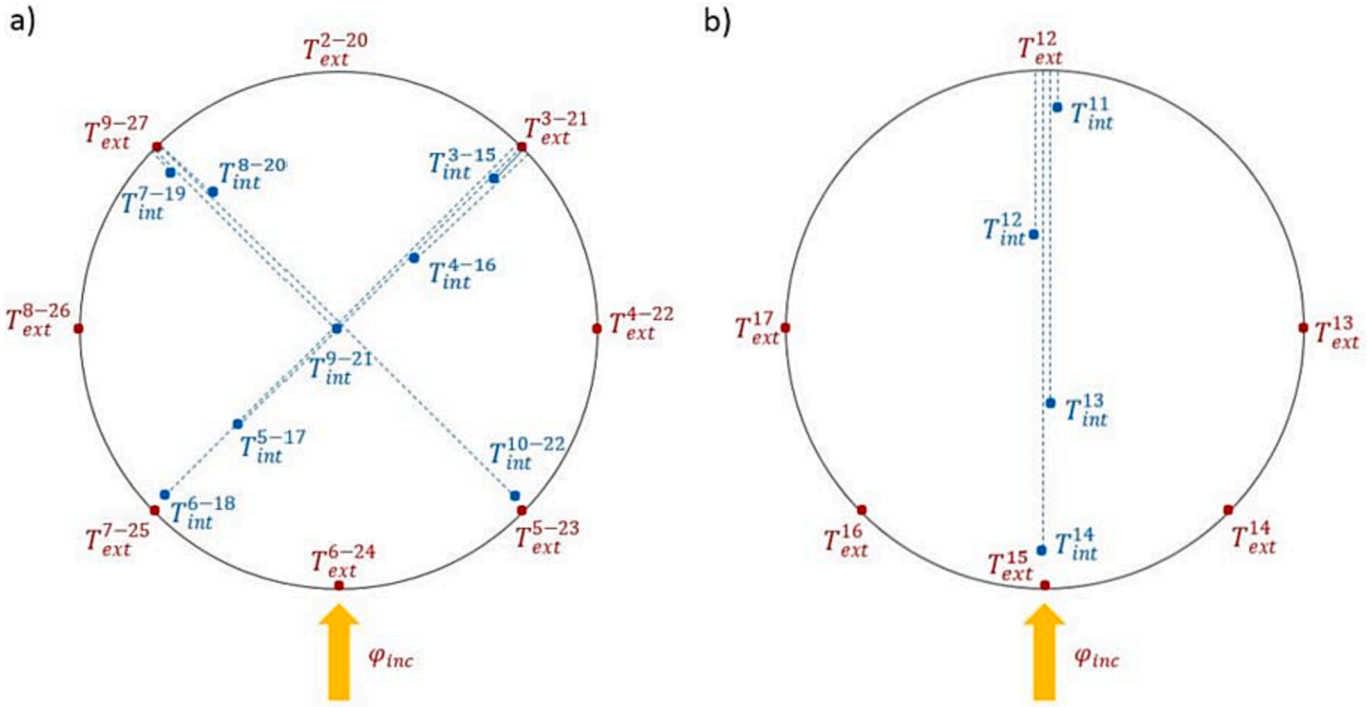

Fig. 3. a) Sections 1 and 3 of thermocouples, at 0.6 and 1.6 m above the aeration respectively that delimitates the irradiated zone, and b) Section 2 of thermocouples at 1.1 m above the aeration at the middle of the irradiated zone.

respectively measure the particle volume fraction and identify the fluidization regime using various signal processing methods that are detailed in [29].

Furthermore, the system is instrumented with 59 K-type thermocouples. In a gas-particle fluidized bed, the thermocouple (TC) arrays can modify the gas-particle flow since the diameter of the TC is approximately 25 times the particles one. Nevertheless, this disturbance influences mainly the flow downstream and, consequently, the TC

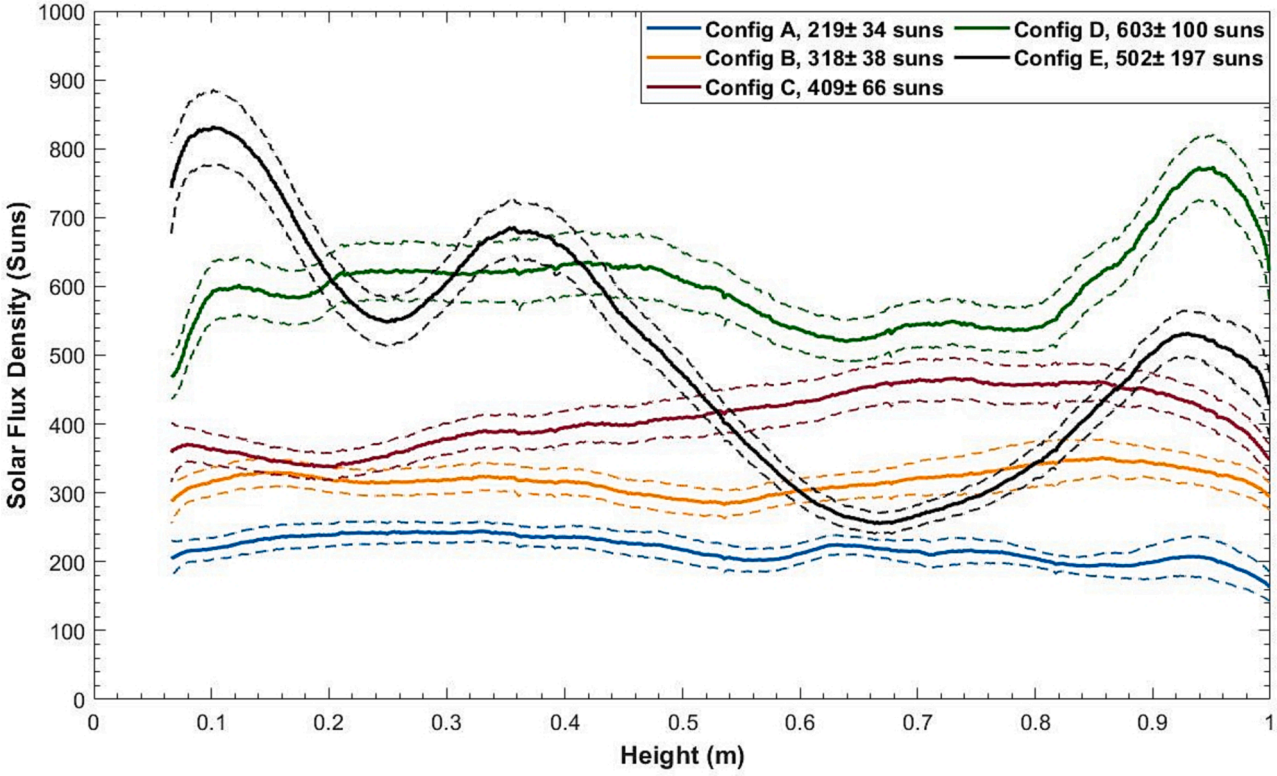

Fig. 4. Measured solar flux distributions used for the experimental campaign. The mean values range between 200 and 600 suns, while local value is measured up to 830 suns.

measurement is a little affected. Another source of uncertainty can be the imperfect contact between the particles and the TC. This issue is not considered as significant since, in fluidized beds, the gas and the solid phase are at the same temperature thanks to the efficient particle mixing and the large surface area of small size powders. Consequently, the temperature measured by the thermocouples is the temperature of both the air and the particles [25]. Moreover, the small particle size favors the contact with any immersed surface. Three thermocouples are dedicated to the measurement of the mean particle temperature in the dispenser, T_{disp}. In the receiver tube, 24 thermocouples indicate the local particle temperature and 32 thermocouples are welded on the outside walls to measure the external tube temperatures. All of them are represented in blue and red respectively in both Fig. 1 and Fig. 3. Three cross sections of the tube are fully instrumented as represented in Fig. 3a-b. They are located at the entrance, the middle and at the end of the irradiated zone of the tube, as identified with green dashed lines on Fig. 1.

The precise positions of the pressure probes and thermocouples in the receiver tube are detailed in Appendix A.

2.4. Concentrated solar flux

The experimental set-up is placed at the focus of the 1 MW solar furnace of CNRS (Odeillo, France). The sun light is reflected twice before reaching the receiver: the first reflection is performed by the heliostats field while the second is performed by the parabola [30,47]. A schematic representation of the working principle is given in Supplementary Information SI-1. To achieve the solar flux distributions, the tracking setpoint of the heliostats were modified to widen the focus of the parabola and illuminate the receiver tube with the best solar irradiation homogeneity. The chosen method consists in acquiring images of a previously calibrated diffusing surface. This method therefore comprises two steps: calibration and image acquisition. To carry out the calibration, a calorimeter is positioned at the location of the solar receiver. One or more heliostats are used to achieve the selected flux densities. Then, an alumina coated (deposited by plasma) aluminum bar is placed inside the cavity of the receiver, at the position of the cavity aperture, and water-cooled. A camera placed in front of the receiver – at a distance of 18 m – provides images of the bar illuminated by the heliostats. These images enable establishing a grayscale-flux correspondence. The next step consists in activating the heliostats in tracking position according to the solar flux density they provide as well as their geometrical distributions (shape at the focus). Five heliostats configurations have been obtained that correspond to maps of the solar flux density distribution at the cavity aperture. Then, a mean value of the flux density is calculated at each height over the larger, and an associated uncertainty is calculated as the sum of the measurement error and of the standard deviation of the measured values. The five distributions are presented in Fig. 4. As the total solar flux density depends on the direct normal irradiation (DNI), the distributions are presented in the figure in terms of concentration ratios, i.e. expressed in suns. The dashed lines are representative of the uncertainties. For each configuration, a mean value can be calculated that varies between 220 and 600 suns. It is associated to an uncertainty calculated as the sum of the calculation error and of the standard deviation of the distribution, then representative of the homogeneity over the height. These values are indicated in the legend of the figure.

Fig. 4 indicates that although the A and B distributions are relatively constant over the height, the C and D distributions – at higher mean solar flux – are less homogenous. Actually, it is difficult to obtain homogeneous high flux configurations over 1-meter height with the solar furnace because such a solar facility is usually designed to obtain a very high concentration ratio (up to 10,000) on small areas [3]. A solar tower is more adapted to deliver this type of distribution for a scaled-up receiver [5,46]. The E distribution (in black in the figure) has been

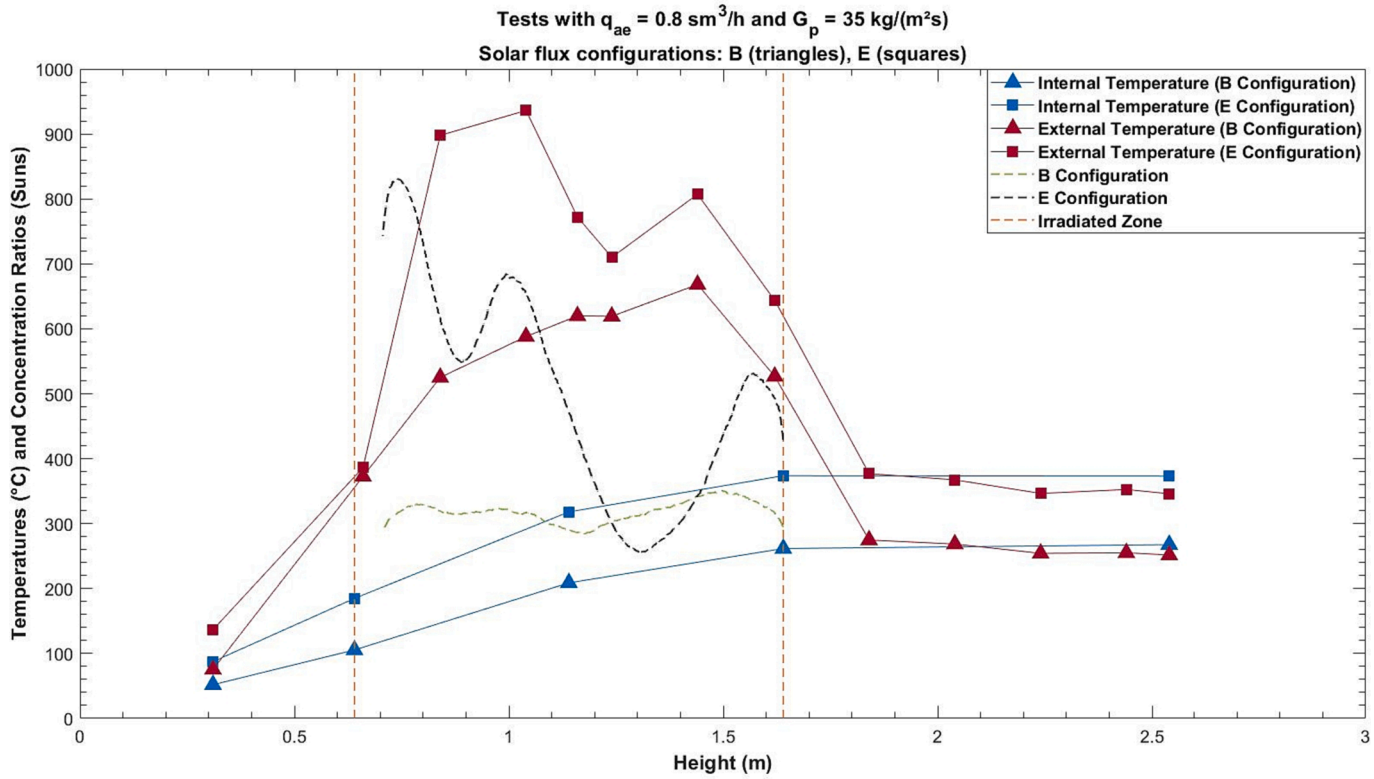

Fig. 5. Temperature distributions with respect to the height: front wall (red) and particle (blue) temperatures, for the B and E solar flux configurations (triangles and squares respectively). The associated flux distributions are respectively in green (B) and black (E). The aeration flow rate and the particle mass flux are identical for both cases and respectively equal to 0.8 sm^3/h and 35 $kg/(m^2s)$. (For interpretation of the references to color in this figure legend, the reader is referred to the web version of this article.)

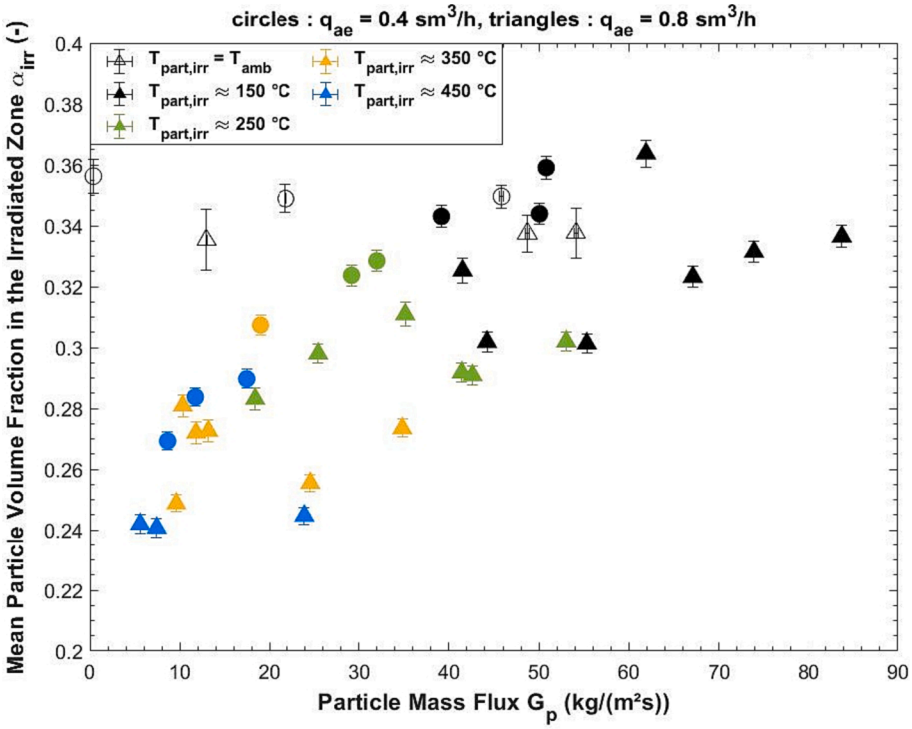

Fig. 6. Evolution of the mean particle volume fraction in the irradiated zone as a function of the particle mass flux, for aeration flow rates of 0.4 (circles) and 0.8 (triangles) sm^3/h, and for various particle temperatures.

selected to test the sensitivity of the system to strong flux density differences along the height, with similar total incident power than the D distribution. The maximum is at 830 suns at the bottom of the receiver, and the minimum, at 255 suns.

3. Results

A total of 187 tests have been performed in stationary conditions in terms of particle mass flux, pressure and temperature, using a large range of experimental parameters. The associated results are presented in this section.

3.1. Control of the solar power plant

3.1.1. Operating parameters

The experimental setup can be controlled thanks to three parameters:

- The total relative pressure in the dispenser, P_{tot}, which imposes the driven pressure gradient. It ranges from 145 to 380 mbar in the reported experiment.
- The aeration flow rate, $\dot{q_{ae}}$, which enables finely tuning the particle mass flow rate and the fluidization regimes. The later ranges from 0.1 to 2.5 sm^3/h in the reported experiment, which corresponds to superficial air velocity in the tube between 0.025 and 0.469 m/s.
- The incoming concentrated solar flux density that imposes the thermal load of the receiver. According to the solar flux density distributions presented above and the variations of the DNI during the experiments – between 750 and 1030 W/m^2 – the net incident solar power on the receiver ϕ_{sol} varies between 19 and 56 kW.

By adjusting the previous parameters, the operating point of the receiver can be prescribed. The first operating characteristic is the particle mass flow rate, $\dot{m}_p$. Experimentally, it is calculated by linear regression of the particle mass flowing on the weighing scale over time. The uncertainty associated with this measurement is due to both the regression error and the accuracy of the scale (0.01 kg for data recorded at 10 Hz). In the field of fluidization, the particle mass flux G_p is more classically used. It corresponds to the particle mass flow rate normalized by the internal section of the tube. It varies between 0 and 93 $kg/(m^2s)$ during the experimental campaign, that corresponds to a particle mass flow rate of 0.17 kg/s, or 613 kg/h. An example of the evolution of the particle mass flux with respect to the total pressure in the dispenser and for various aeration flow rates and incident solar flux densities is given in Supplementary Information SI-2. Increasing the solar flux leads to a decrease of the total pressure required to reach a given particle mass flux. This behavior is mostly due to the temperature increase, which results in a decrease of the particle volume fraction, α. The same trend is observed when increasing the aeration flow rate, as observed at ambient temperature in [28]. This point is discussed in the next section.

The second important characteristic of the solar receiver is the particle temperature. To characterize the suspension temperature from a global point of view, an average temperature is calculated over the irradiated zone, $T_{part,irr}$. According to the results, this average is very similar to the value of the particle temperature at the middle of the irradiated zone. Then, to facilitate the calculations, only the latter is considered. The average temperature is calculated by Equation (2), and the positions of T_{int}^{12} and T_{int}^{13} are presented in Fig. 3b (the two sensors are located 1.1 m above the aeration, at radial positions of respectively $D_t/3$ and $2D_t/3$).

$$T_{part,irr} = \frac{T_{int}^{12} + T_{int}^{13}}{2} \tag{2}$$

Fig. 5 presents the particle and front wall temperatures distributions along the tube height for two similar tests done with 0.8 sm^3/h of aeration flow rate and 35 $kg/(m^2s)$ of particle mass flux, for the B and E solar flux density configurations, identified respectively with the triangles and squares. In the irradiated zone, delimited in the figure by the vertical dashed lines, the wall temperatures profiles (red) follow the shapes of the solar flux distributions (green and black respectively for the B and E configurations), while the particle temperatures (blue)

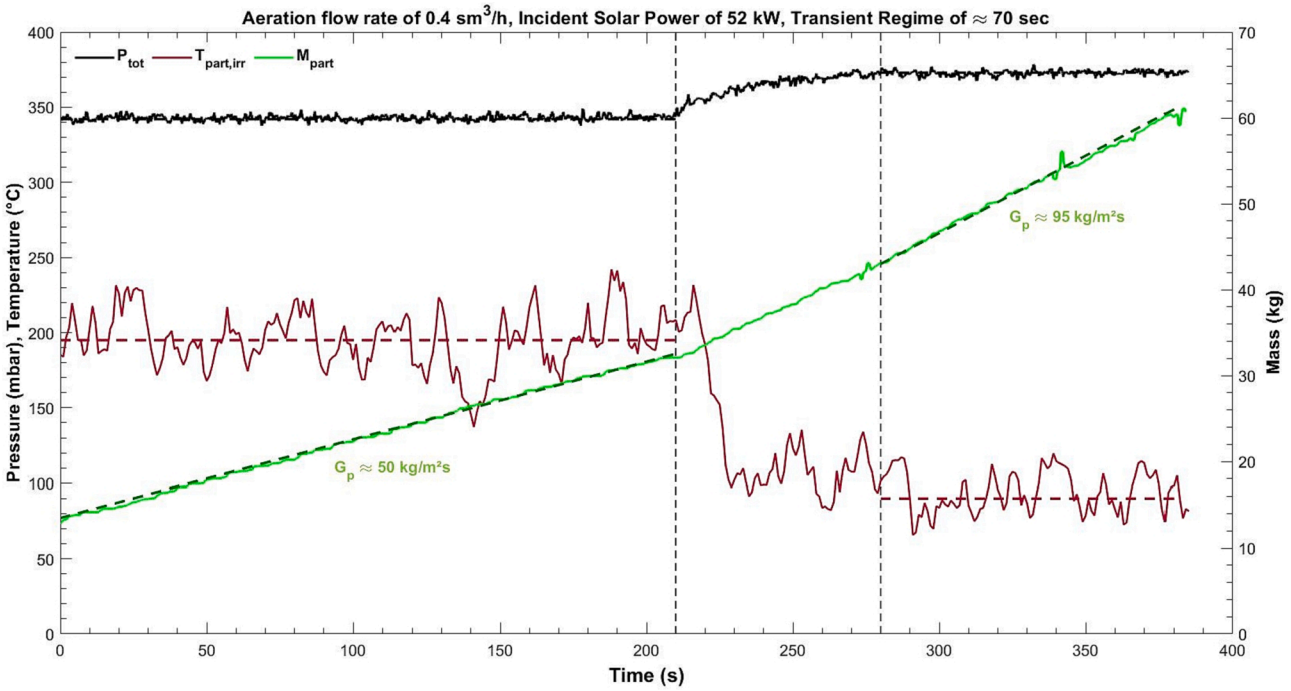

Fig. 7. Time evolutions of the particle temperature inside the irradiated zone (red), the particle mass flux (green) after an increase of the pressure in the dispenser (black) and for a constant aeration flow rate. (For interpretation of the references to color in this figure legend, the reader is referred to the web version of this article.)

increase with the height due to the internal mixing. In these examples, although the particles are at ambient temperature in the dispenser – around 20 °C – they are already heated at their entrance in the irradiated zone. This is related to the reflux of the particles at the tube walls, previously highlighted by [7], and to conduction in the tube walls.

3.1.2. Particle volume fraction

Since the HTF is composed of air and particles, a change of the operating parameters may lead to a change of the effective density, which depends on the particle volume fraction, α. A special concern is thus dedicated to the evolution of this quantity. The particle volume fraction is the fraction occupied by the particles in a given control volume, calculated with Equation (3). It is measured thanks to the differential pressure ΔP between two successive pressure probes, spaced by Δh along the tube height. Neglecting the pressure drop terms related to the acceleration and friction of the particles, α is directly due to the relative weight of the suspension [22,50].

For the sake of clarity, an average volume fraction is calculated inside the irradiated zone, α_{irr}, i.e. between the pressure probes $P2$ and $P5$ (cf. Fig. 1).

$$\alpha = \frac{\Delta P}{(\rho_{part} - \rho_{air}) g \Delta h} \tag{3}$$

Fig. 6 represents the evolution of α_{irr} as a function of the particle mass flux G_p, for two aeration flow rates: 0.4 (circles) and 0.8 (triangles) sm^3/h. The marker colors are representative of the mean particle temperature $T_{part,irr}$. Previous works [29,28] have shown that at ambient temperature, α decreases quasi-linearly with the aeration flow rate and slightly depends on the particle mass flux, as observed here by the empty markers on the figure. However, for a given aeration flow rate, the trend is significantly different when the system is irradiated. For example, at ambient temperature and 0.8 sm^3/h of $\dot{q_{ae}}$, the particle volume fraction slightly varied between 0.31 and 0.33 for a particle mass flux ranging from 0 to 90 kg/(m^{2}s). With particles temperature between 150 and 450 °C and the same aeration flow rate, α_{irr} ranges here from 0.24 to 0.33 in the same range of particle mass flux. This Figure also highlights that the particle volume fraction decreases with the temperature. A more detailed evolution of α_{irr} as a function of the superficial air velocity and the particle temperature is presented in Supplementary Information SI-3.

3.1.3. Transient regime

A change of one of the control parameter, for example a change of DNI induced by cloud passing, involves a transient response of the system. The management of such event is of paramount importance to optimize control, operation security, and performances of future large-scale particle receiver. In the following section, the effect of different parameters on the transient response of the system is discussed.

Fig. 7 presents the transient response of the system to a variation of the dispenser pressure, for a constant aeration flow rate of 0.4 sm^3/h and an incident solar power of 52 kW (using the D solar flux configuration). The test starts with stationary conditions in terms of the particle temperature in the irradiated zone $T_{part,irr}$ (in red) and of the particle mass flux G_p (linear regression of the particle mass M_{part} in green). At $t = 210$ s, the dispenser pressure increases by closing the leak valve. As a results, the pressure P_{tot} (in black) rises from 340 to 375 mbar. The transient duration, defined as the time required for the pressure to reach 95 % of the pressure variation, is equal to 70 s. The latter is identified on the figure by the vertical dashed lines.

Without particle circulation, an increase of the pressure in the dispenser induces a rise of the suspension height. When the suspension flows, the height cannot be adjusted, thus the dispenser pressure increase results in an increase of the particle mass flow rate. The latter is identified in Fig. 7 by a slope change in the mass weighted by the scale (green curve). For on-sun operation, the particle mass flux increase results in a decrease of the particle temperature. For this test, a slight change of pressure – a 10 % increase in this example – led to a 90 % relative increase of the particle mass flux (from 50 to 95 kg/(m^{2}s)) and to a 54 % relative decrease of the particle temperature (from 195 to 90 °C). From a process control point of view, the power plant operator could thus use a pressure based control in case of “strong variation”

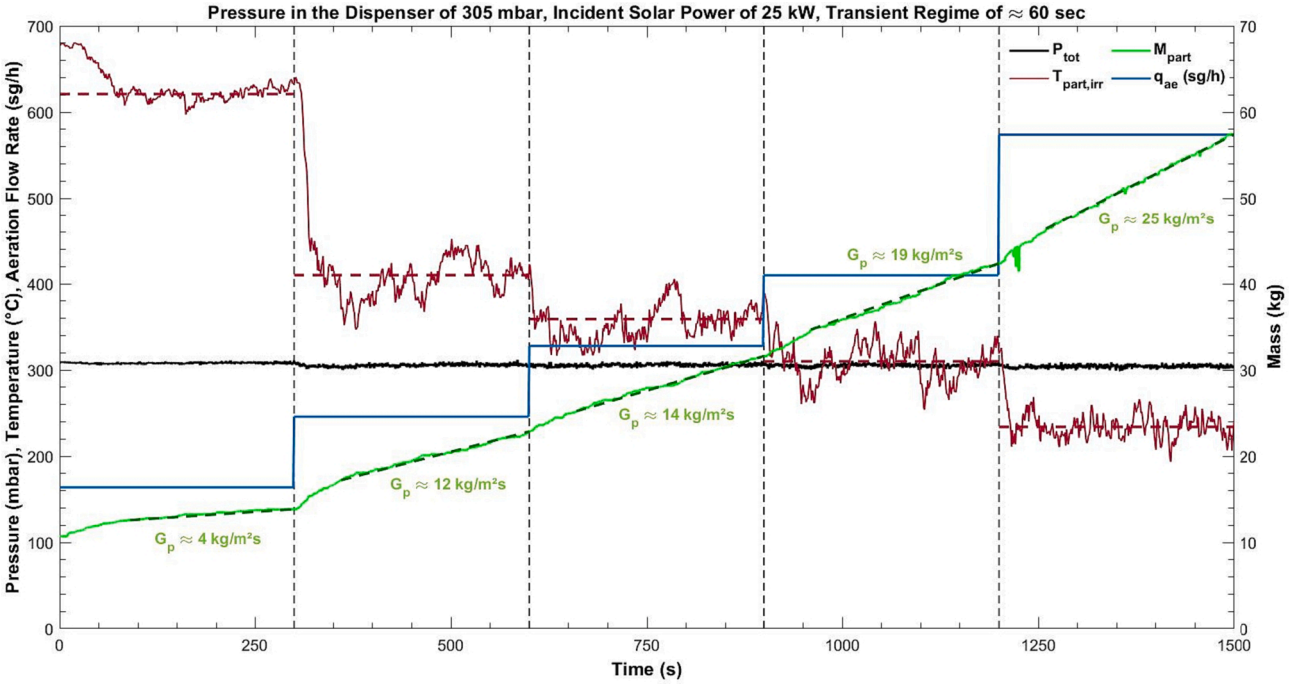

Fig. 8. Temporal evolutions of the particle temperature inside the irradiated zone (red), the particle mass flux (green) after an increase of the aeration flow rate (blue) and for a constant pressure in the dispenser (black). (For interpretation of the references to color in this figure legend, the reader is referred to the web version of this article.)

events.

Fig. 8 shows the response of the system to an aeration flow rate variation, with a constant pressure in the dispenser of 305 mbar, and a constant incident solar power of 25 kW (the B solar flux configuration). The initial steady state corresponds to a particle temperature in the irradiated zone $T_{part,irr}$ (in red), a particle mass flux G_p (in green) and an aeration flow rate (blue), expressed in sg/h instead of sm^3/h to fit with the scale of the figure. At $t = 300$ s, the aeration flow rate increases from 0.16 to 0.24 sm^3/h. Successive aeration mass flow rate changes are presented on the figure. The starting time of each transient is illustrated by a vertical dashed line. The air flow rate rise induces a dilution of the suspension, i.e. a decrease of the particle volume fraction α. As a first approximation, the particle volume fraction over the tube height is proportional to P_{tot} (the pressure drop over the height of the tube) according to Eq.(3). As the driving pressure of the flow (i.e. P_{tot}) remains constant during the test, a reduction of α results in an increase of the particle mass flux to respect the pressure balance. As in Fig. 7, the mass flow rise is characterized by an increase of the slope of the particle mass variation after each increase of $\dot{q_{ae}}$. Assuming a constant incident solar power, the mass flux rise induces a decrease of the temperature. As discussed before (Section 3.1.2), for a given aeration flow rate and particle mass flux, when $T_{part,irr}$ decreases, the particle volume fraction increases. This sequence highlights a self-regulation behavior of the system that oscillates around its new equilibrium before stabilizing. In Fig. 8, five successive steady states induced by five successive increases of the aeration flow rate are illustrated. For each sequence, the self-regulation duration lasts approximately 60 s and can be summarized as follows.

$$\dot{q_{ae}}\nearrow \Rightarrow \alpha_{irr}\searrow \Rightarrow G_p\nearrow \Rightarrow T_{part,irr}\searrow \Rightarrow \alpha_{irr}\nearrow$$

Between the first and the second sequence, a very strong decrease of the particle temperature occurs due to a very low initial particle mass flux. Between the second and the third sequence, the aeration flow rate increases from 0.24 to 0.32 sm^3/h, i.e. a relative increase of 33 %. This strong variation of the control parameter results in small relative variations of the particle temperature and mass flux, respectively of 12 % (from 410 to 360 °C) and 16 % (from 12 to 14 $kg/(m^2s)$). To summarize, from a process control point of view, the power plant operator could thus use an aeration flow-based control to finely adjust the operating conditions.

Table 3
Response of the system from an increase of the pressure in the dispenser and of the aeration flow rate.

Increase of the operating parameter		Consequences		
		Particle mass flux Increase	Particle mass flux Increase	Duration of the transient regime
Pressure	10 % From 340 to 375 mbar	90 % From 50 to 95 $kg/(m^2s)$	54 % From 195 to 90 °C	70 s
Aeration flow rate	33 % From 0.24 to 0.32 sm^3/h	16 % From 12 to 14 $kg/(m^2s)$	12 % From 410 to 360 °C	60 s

The responses of the system to an increase of the pressure and the aeration flow rate are summarized in Table 3.

3.2. Thermal performances of the receiver

3.2.1. Absorbed power

The particle temperature increase in the solar receiver is given by $\Delta T_{part} = T_{part}^{out} - T_{disp}$. The particle outlet temperature, T_{part}^{out}, is given in Equation (4). It is calculated as the average of the particle temperature measured within the tube at the outlet of the irradiated zone, at radial positions of $D_t/3$, $D_t/2$ and $2D_t/3$ (cf. Fig. 3a). However, the particle inlet temperature is not measured at the inlet of the irradiated zone, because the particles are already heated due mainly to the reflux at the tube walls [7]. To account for these effects on the measurements and describe the real increase due to the solar irradiation, the temperature in the dispenser T_{disp} is used. During the experimental campaign, the

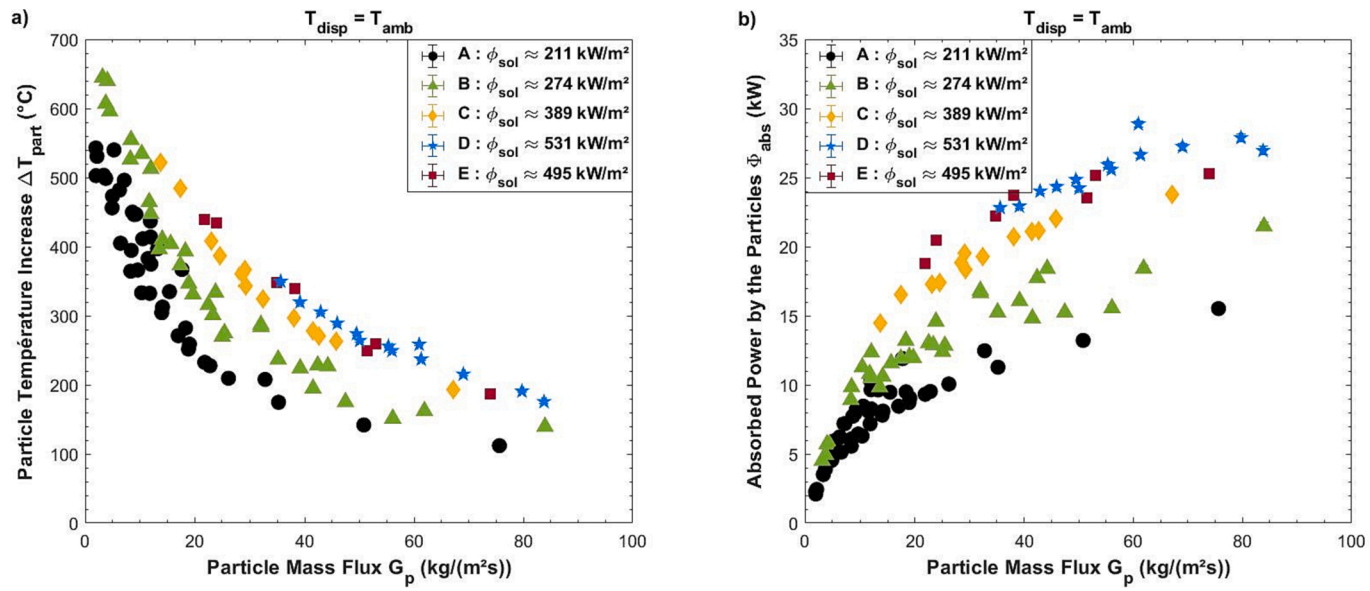

Fig. 9. Evolutions of a) the increase of the particle temperature, and b) the absorbed power by the particles, as a function of the particle mass flux and for various incident solar flux densities.

temperature increase ΔT_{part} ranges between 105 and 645 °C, as shown in Fig. 9a as a function of the particle mass flux.

Fig. 9b shows the evolution of the absorbed power by the particles ϕ_{abs}, calculated by Equation (5) with respect to the particle mass flux. In this Equation, $C_{p,part}$ is calculated as a function of the mean particle temperature in the irradiated zone, $T_{part,irr}$ (cf. Equations (1)–(2)). Since, the particles belong to the class A of the Geldart classification [23], the air velocities needed to fluidize them (and vary the fluidization regimes) are low. Consequently, the absorbed power by the air represents less than two percent of the power absorbed by the particles. This quantity is thus negligible in the power balance [43].

In Fig. 9a-b, the various markers and colors are representative of the incident concentrated solar flux density, i.e. the product of the concentration ratio and the DNI. For all the tests, the dispenser is at ambient temperature, ~25 °C. The bars amplitudes indicate the measurement and calculations errors of the particle mass flux and of the particle temperatures.

$$T_{part}^{out} = \frac{T_{int}^{16} + T_{int}^{17} + T_{int}^{21}}{3} \tag{4}$$

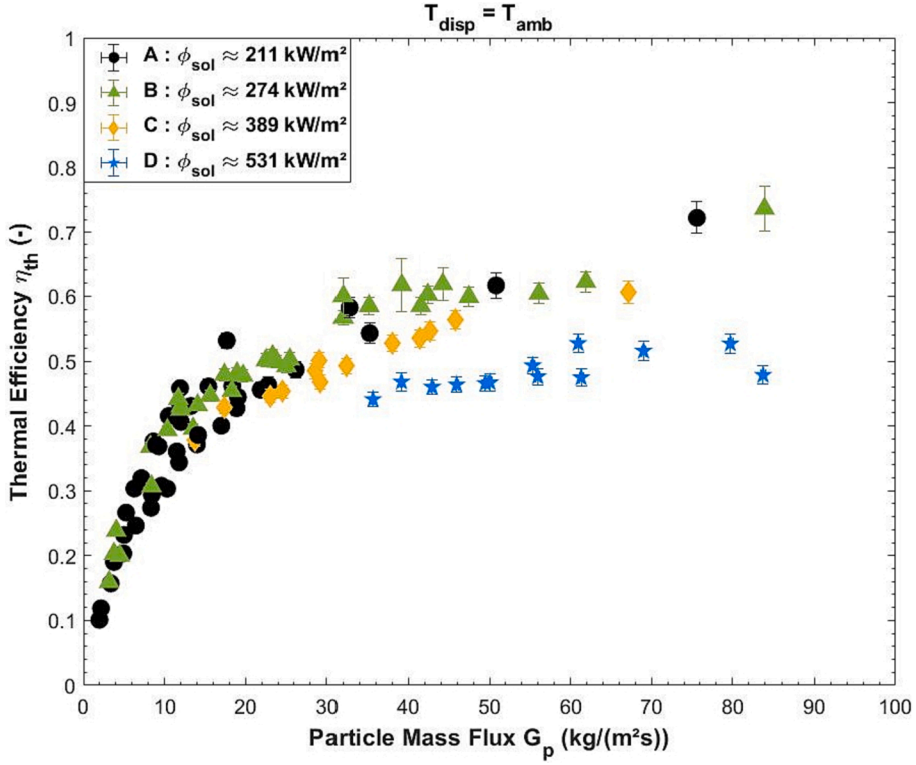

Fig. 10. Evolution of the thermal receiver efficiency as a function of the particle mass flux and for various incident solar flux densities.

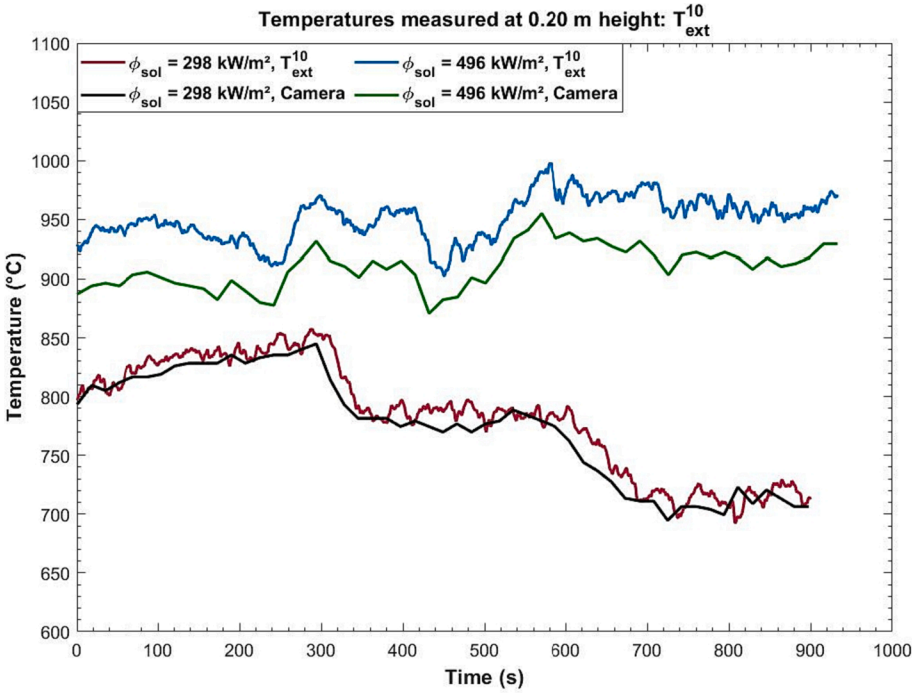

Fig. 11. Comparisons of the temperatures measured by the thermocouple T_{ext}^{10} and the infrared camera, at 0.84 m height, for two solar flux configurations.

$$\phi_{abs} = \dot{m}_p C_{p,part}\left(T_{part}^{out} - T_{disp}\right) \quad (5)$$

Figrrrure 9a-b illustrates that, for a given solar power, increasing the particle mass flux leads to an increase of the absorbed power by the particles and a decrease of the particle temperature. This is directly related to the particle mean residence time in the irradiated part of the tube. For example, for a particle mass flux of 2 kg/(m^{2}s), the mean residence time is approximately 400 s and corresponds to a temperature increase of 530 °C, while for a particle mass flux of 93 kg/(m^{2}s), it drops to respectively 7.5 s and 105 °C. Furthermore, for a given G_p, increasing the solar power leads to an increase of the wall and particles temperature, and finally of the absorbed power.

Despite very high peak in terms of concentration ratio for the E solar flux configuration (above 800 suns) the maximum tube wall temperature remains below 1000 °C. Compared to the D configuration, the particle temperature increase is very similar but the wall temperature distribution is very different (cf. Section 2.4). It means that from the particle temperature increase view point, only the total energy received on the aperture of the cavity matters. Since the E configuration is a limiting case that results in very high wall temperature gradient and heterogeneity, is not taken into account anymore in the following result analysis.

3.2.2. Thermal efficiency

The thermal efficiency of the receiver, η_{th}, represents the ratio of the absorbed power over the incident solar power, as presented in Equation (6). Fig. 10 presents the variation of η_{th} with respect to the particle mass flux. The trend is logically similar to the one presented for the absorbed power. Increasing the particle mass flux leads to an asymptotic increase of the receiver thermal efficiency which seems to converges for mass flux above 30 – 40 kg/(m^{2}s). This finding agrees with the data of [38] with one finned tube. However, the efficiencies obtained in this latter work were slightly higher (of approximately 5 % for all the solar configurations tested) due to the higher exchange surface between the hot tube and the particles. Considering the small increase in efficiency, the addition of fins within the tube of the particle-in-tube solar receiver seems to be not worthy. Furthermore, the efficiency was much higher (between 0.85 and 90 for particle mass flux around 40 kg/(m^{2}s)) in the earlier study with 16 bare tubes tanks to the cavity effect [43].

$$\eta_{th} = \frac{\phi_{abs}}{\phi_{sol}} \quad (6)$$

Fig. 9 and Fig. 10 presented above highlight the need of combining high particle mass flux and high incident solar power to obtain both high particle outlet temperature and high thermal efficiency. Results are obtained with particle inlet temperature at the ambient. Additional experiments have been performed with preheated particles in the dispenser, with temperature ranging from 100 to 300 °C. The results are presented in Supplementary Information SI-4. For given particle mass flux and incident solar flux, preheating the particles leads, as expected, to higher particle outlet temperature. Nevertheless, as the temperature increases, the thermal losses – mostly radiative – increase too, which leads to a decrease of the absorbed power and thus to the thermal efficiency.

3.3. Heat transfer

3.3.1. Global heat transfer coefficient

To characterize the heat transfer between the internal walls of the tube and the particles over all the irradiated zone height, a global wall-to-particles heat transfer coefficient, $h_{wall,part}$, is calculated with Equation (7) [7,38]. The latter is similar to the classical formulation of convective exchange in a heat exchanger. Since $h_{wall,part}$ aims to quantify the way the concentrated heat power is transferred to the particle in the irradiated part of the tube, the considered exchange area is half of the internal cylinder surface, $S_{exch} = \pi D_t H_{irr}/2$.

To consider the variations of the wall to particle temperature difference over the tube height, a logarithmic mean value is considered between the inlet and the outlet of the irradiated zone, $\Delta T_{wall,part}$ (Equation (8)). The associated uncertainties are detailed in Appendix B.

$$h_{wall,part} = \frac{\phi_{abs}}{S_{exch}\Delta T_{wall,part}} \quad (7)$$

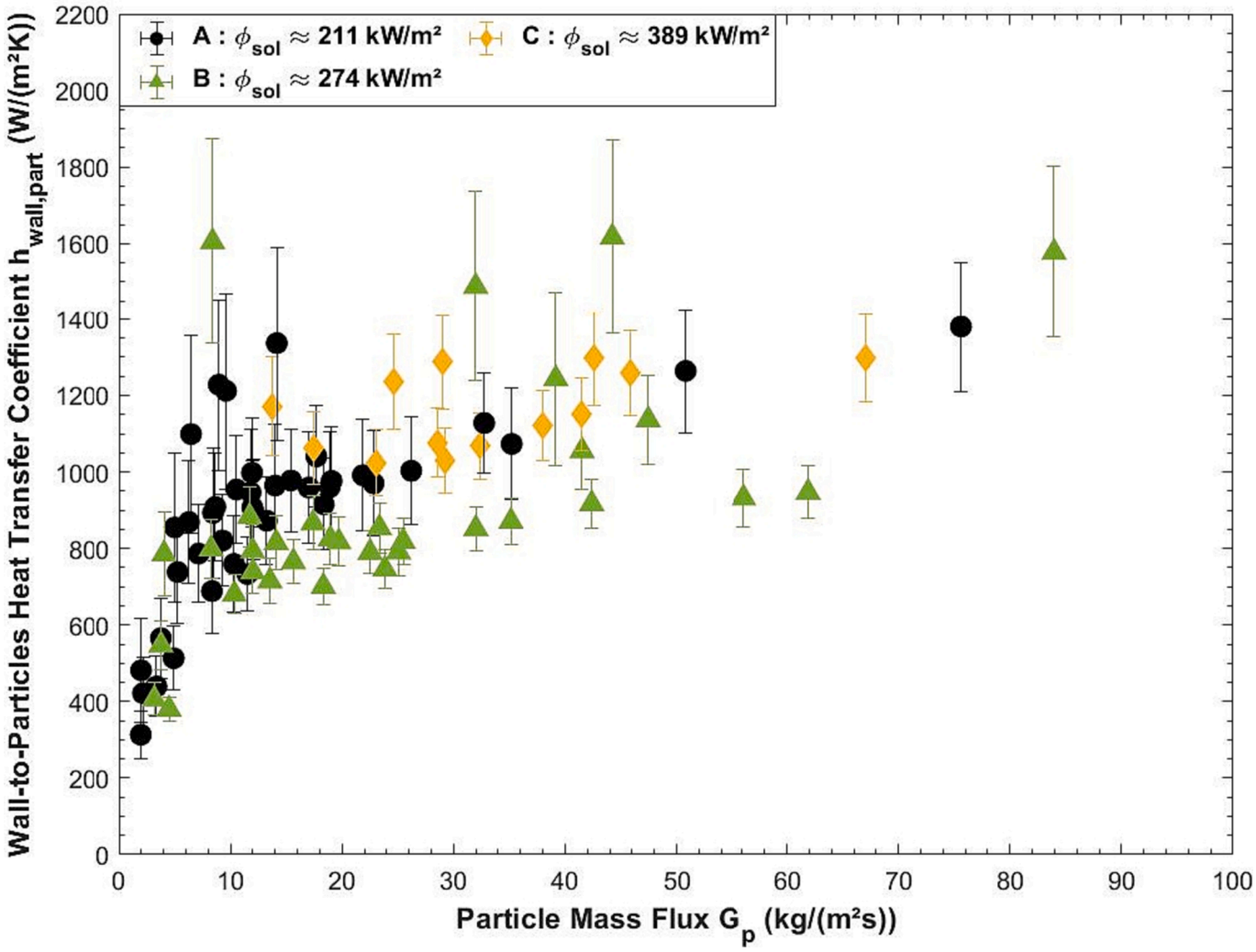

Fig. 12. Evolution of the wall-to-particles heat transfer coefficient as a function of the particle mass flux and for various incident solar flux densities.

$$\Delta T_{wall,part} = \frac{\left(T^{in}_{wall,int} - T^{in}_{part}\right) - \left(T^{out}_{wall,int} - T^{out}_{part}\right)}{\ln\left(\frac{T^{in}_{wall,int} - T^{in}_{part}}{T^{out}_{wall,int} - T^{out}_{part}}\right)} \tag{8}$$

For this calculation, the particle inlet temperature considered is not anymore the dispenser temperature but an average of the recorded temperature at the inlet of the irradiated zone, T^{in}_{part} (Equation (9)). The internal wall temperatures, $T^{in}_{wall,int}$ and $T^{out}_{wall,int}$, are estimated based on the measurement performed on the external walls and considering the heat conduction trough the tube (Equation (10)). In the equation, the mean solar flux density φ_{sol} is given by the solar flux distributions, $\alpha_{pyro} = 0.85$ is the absorptivity of the Pyromark® paint in the solar wavelengths ("Alloy Wire International, Inconel 601," 2020; [33], and $\lambda_{inconel}$ is the thermal conductivity of the Inconel® material ("Alloy Wire International, Inconel 601," 2020). The latest is given by Equation (11) with T the temperature in °C. Finally, the external wall temperatures, $T^{in}_{wall,ext}$ and $T^{out}_{wall,ext}$, are measured by the welded thermocouples (cf. Section 2.3).

$$T^{in}_{part} = \frac{T^{4}_{int} + T^{5}_{int} + T^{9}_{int}}{3} \tag{9}$$

$$T^{in,out}_{wall,int} = T^{in,out}_{wall,ext} - \frac{e_t}{\lambda_{inconel}} \alpha_{pyro} \varphi_{sol} \tag{10}$$

$$\lambda_{inconel} = 0,0169{*}T + 10,95 \tag{11}$$

However, previous experiments have highlighted the difficulty to measure precisely the temperatures with externally welded thermocouples [38]. For on-sun experiment, when the welded thermocouple is exposed to high concentrated solar flux, its temperature may be higher than the tube walls due to the thermal resistance between the weld and the surface. Consequently, the temperature must be corrected. A second measurement were performed using an infrared camera placed in front of the receiver (at 18 m of the focus of the parabola) to estimate the measurement error due to the thermal resistance. A comparison of the two measurement results, at the location of the thermocouple T^{10}_{ext} (0.84 m above the aeration injection), is presented in Fig. 11 for two solar flux configurations. The temperature is post-processed from the camera image using an emissivity of 0.85. For relatively low solar flux density, the temperature given by the two measurement agrees very well. However, for high solar flux density, the temperature given by the thermocouple (blue) is overestimated compared to the temperature given by the camera (green) by approximately 50 °C.

Then, experiments were performed with the infrared camera to compare the temperatures given by the thermocouples at various height of the tube. Nevertheless, it is experimentally difficult to extract significant trend of the temperature difference versus the solar flux because several parameters can affect the temperature given by the camera. First, the emissivity of the tube can vary along the tube height. Second,

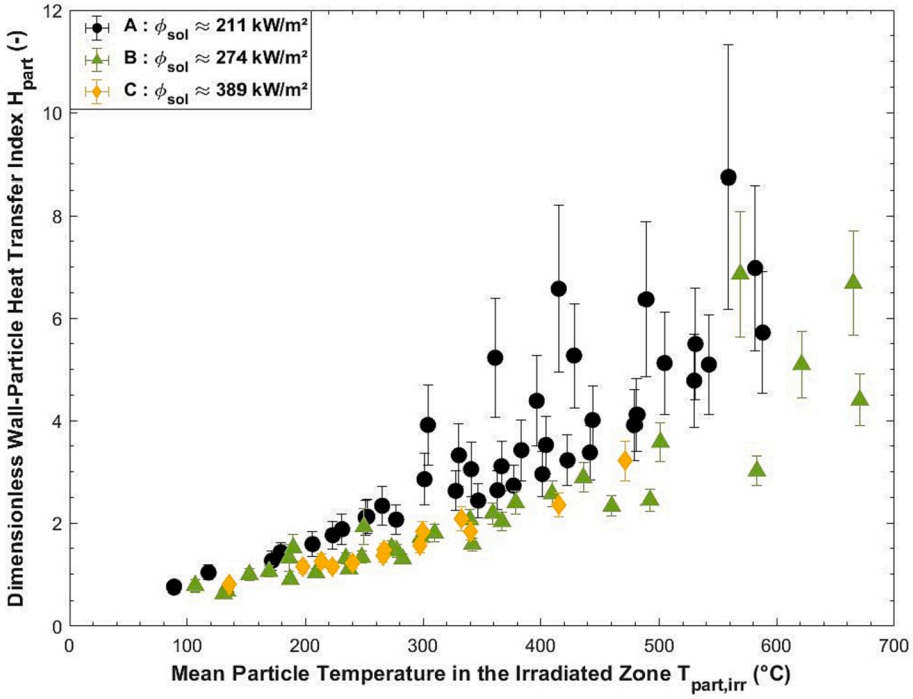

Fig. 13. Evolution of the dimensionless wall-to-particle heat transfer index as a function of the mean particle temperature in the irradiated zone, and for various incident solar flux densities.

the resolution of the camera limits the spatial accuracy of the measurement at 1 pix/cm. Third, the external welded thermocouples have white ceramic sheaths (as shown in Fig. 2a) that may be recorded by the camera and result in wrong local data. As the temperatures measured by the thermocouples are always higher than the temperatures measured by the IR camera and the difference varies with the solar flux density, we chose to decrease the measured data by a mean value of 25 °C. It is associated to a constant uncertainty of 25 °C.

Fig. 12 presents the evolution of the global wall-to-particles heat transfer coefficient as a function of the particle mass flux, for three incident solar flux densities. Due to the strong heterogeneities of the D and E solar distributions, they are not presented in the figure.

According to Equation (7), $h_{wall,part}$ varies similarly to the absorbed power by the particles. Since the extracted power by the particles increases with the particle mass flux as does $h_{wall,part}$. A plateau is reached when the increase in the temperature difference between the wall and the fluidized bed compensates the previous trend. The calculated values are consistent with previous studies. For examples, [38] obtained mean heat transfer coefficients of 1200 ± 400 W/(m^{2}K) with a finned tube, for particle mass flux higher than 40 kg/(m^{2}s) and solar flux density of 236 kW/m^2. Logically, this value is higher than the one obtained in the present study in similar operating conditions (for homogeneous solar flux configurations A et B) since fins enhance heat exchange area. Furthermore, with silicon carbide particles and one bare tube, [7] measured mean coefficients of 800–900 W/(m^{2}K) for particle mass flux in the range 30–40 kg/(m^{2}s) and solar flux density of 387 kW/m^2. The operation conditions correspond to the C solar flux configuration, for which the measured values of $h_{wall,part}$ are slightly higher in the present study. The main difference between the two experiments is the irradiated length of the tube, that was 0.5 m for [7].

As a conclusion, according to Fig. 12, the global wall-to-particle heat transfer coefficient varies mainly with the particle mass flux. It reaches a quasi-plateau above 15 kg/(m^{2}s) with a mean value of 1000 ± 200 W/(m^{2}K) and some peaks data up to 1500 W/(m^{2}K). However, it is difficult to extract the influence of the particle temperature and of the fluidization regime from this global heat transfer coefficient. An alternative approach is discussed in the next section.

3.3.2. *Discussion about the heat transfer*

In an ideal solar receiver, the temperature of the absorber wall is equal to the temperature of the HTF. It corresponds to an infinite heat transfer coefficient between the wall and the HTF. Consequently, the value of the heat transfer coefficient is required to design a solar receiver and to estimate the wall-to-HTF temperature difference, the thermal gradient along and around the tube, the associated thermal stresses and, finally, the lifetime of the component. The main objective being to reach the highest outlet temperature of the HTF with the smallest temperature difference between the irradiated wall and the HTF. From this concern, the heat transfer coefficient is a global quantitative data that does not traduce qualitatively the internal temperature distribution inside the tube from the internal wall to the core of the HTF flow. This data is unknown for fluidized particle flowing in a solar-irradiated tube. Consequently, the following section is an attempt to analyze the quality of the heat transfer as a function of the fluidized particle flow characteristics with the objective to reach high outlet temperature with reduced thermal gradient at the wall-to-particle interface.

A dimensionless quantity, $H_{wall,part}$, is defined in Equation (12). It represents the ratio of the particle temperature increase over the average temperature difference between the internal walls and the particles. For example, if both the particle temperature increase (ΔT_{part}) and the temperature difference between the walls and the particles ($\Delta T_{wall,part}$) are high, it means that the heat is not correctly extracted from the hot tube. Conversely, high values of $H_{wall,part}$ correspond to high temperature increases of the particle with reduced temperature differences between the internal walls and the particle flow. It means that this dimensionless number is an effective indicator of the heat transfer quality.

$$H_{wall,part} = \frac{h_{wall,part} S_{exch}}{G_p S_t C_{p,part}} = \frac{\Delta T_{part}}{\Delta T_{wall,part}} \tag{12}$$

Fig. 13 shows the evolution of the dimensionless index $H_{wall,part}$ as a function of the mean particle temperature in the irradiated zone. It increases with the particle temperature in agreement with [7], despite the

Table 4
Comparisons of the dimensionless heat transfer index for various fluidization regimes, at given mean particle temperature, for aeration flow rate between 0.24 and 0.81 sm^3/h and particle mass flux between 4.4 and 23.1 $kg/(m^2s)$.

Mean Particle Temperature $T_{part,irr}$	Fluidization Regime	Dimensionless Heat Transfer Index H_{part}
343 ± 4 °C	Slugging	1.58 ± 0.13
	Fast Fluidization	1.84 ± 0.18
	Turbulent Fluidization	2.93 ± 0.49
404 ± 7 °C	Slugging	2.57 ± 0.25
	Fast Fluidization	3.35 ± 0.63
	Turbulent Fluidization	4.38 ± 0.88

associated low particle mass flux. Actually, the heat transfer in a fluidized bed is the sum of convective, conductive and radiative components [25]. All of these terms increase with the temperature in classical fluidized beds. Above 500 °C, the radiative component predominates the heat transfer. Furthermore, the highest dimensionless heat transfer indices are obtained for the lowest flux configuration. Two explanations arise. First, at high solar flux, the wall-to-particles temperature difference increases. Second, the lowest flux distribution is the most homogeneous.

The temperature has also an influence on the particle flow. Actually, as discussed in [13], the effect of temperature on fluidized Group A particles flow is related to both macro-scale change of gas properties (density and viscosity) and micro-scale changes. At micro-scale, Geldart's Group A particles are subjected to clustering contrarily to Group B as shown in [39]. Clustering is due to inter-particle forces that are important for small particles (Group A). Nevertheless, in fluidized beds the particle volume fraction decreases (the bed porosity increases) with temperature as shown in [21,27] due to weaker attraction forces. This tendency dominates until the sintering effect becomes significant and results in particles agglomeration. This phenomenon was extensively studied, in particular, in fluidized bed combustion since ashes are subjected to agglomeration [4,40]. In dense granular flows studied for CSP applications [2,37], the increase of the coefficient of interparticle static sliding friction leads to a decrease of the particle steady-state mass flow rate. Since the sintering temperature of olivine is approximately 1450 °C no agglomeration was observed in our fluidized bed experiments.

A detailed analysis of the link between heat transfer and fluidization regimes is out of the scope of this paper, it can be found in [27]. However, some preliminary results can be accessed. Since the dimensionless heat transfer index, $H_{wall,part}$, depends on the particle temperature, it has been fixed at approximately 340 and 400 °C, and the result analysis has been done for tests with aeration flow rates and particle mass fluxes varying respectively in the ranges 0.24 – 0.81 sm^3/h, and 4.4 – 23.1 $kg/(m^2s)$. The fluidization regimes have been identified, and results are presented in Table 4. At a given particle temperature, the slugging regime is associated with the lowest heat transfer coefficient. This is mostly due to the large air structures (slugs) that decrease the particle mixing and slow down the particle flow [14,45]. Conversely, as expected, the turbulent fluidization regime is associated to the best heat transfer. Actually, in this regime, the scission of the air structures is predominant compared to their coalescence, that results in vortices and a strong particle mixing [9,49]. The intermediate regime in terms of heat

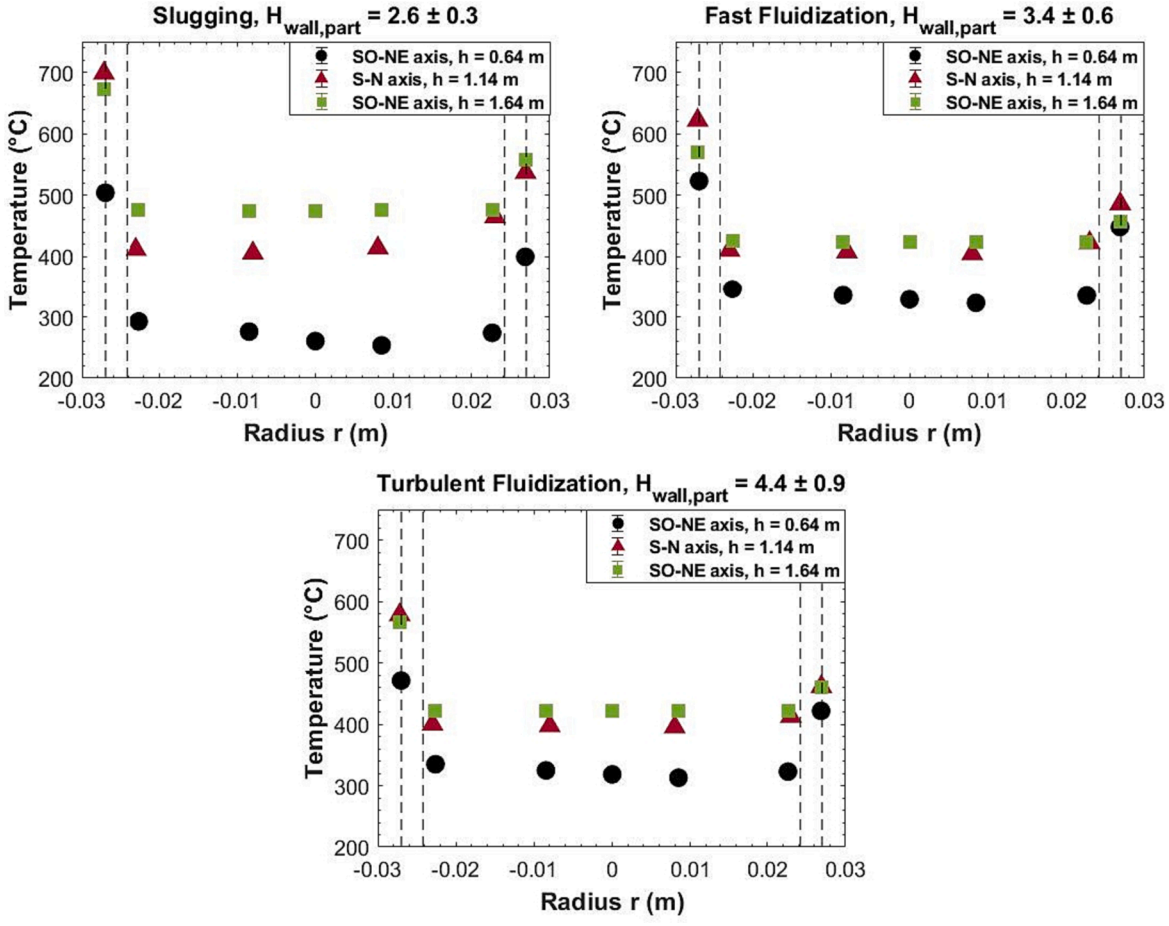

Fig. 14. Evolutions of the temperature with the radius of the tube, at various heights and for various fluidization regimes, for mean particle temperature in the middle of the irradiated zone fixed at approximately 400 °C, and at ambient temperature (around 25 °C) in the dispenser.

Table A1
Heights of the pressure probes implemented on the receiver tube.

N°	$P1$	$P2$	$P3$	$P4$	$P5$	$P6$	$P7$	$P8$	$P9$
Height $z(m)$	0.08	0.84	1.04	1.24	1.44	1.84	2.04	2.24	2.44

Table A2
Positions of the internal and external thermocouples implemented on the receiver tube.

	$x(m)$	$y(m)$	$z(m)$		$x(m)$	$y(m)$	$z(m)$		$x(m)$	$y(m)$	$z(m)$
T_{int}^{1}	0	0	0,31	T_{int}^{20}	−0,015	0,015	1,64	T_{ext}^{15}	0,016	−0,022	1,16
T_{int}^{2}	−0,023	0	0,31	T_{int}^{21}	0	0	1,64	T_{ext}^{16}	0,001	−0,027	1,16
T_{int}^{3}	0,016	0,016	0,64	T_{int}^{22}	0,016	−0,016	1,64	T_{ext}^{17}	−0,020	−0,018	1,16
T_{int}^{4}	0,006	0,006	0,64	T_{int}^{23}	0	0	2,54	T_{ext}^{18}	−0,013	0,024	1,24
T_{int}^{5}	−0,006	−0,006	0,64	T_{int}^{24}	−0,023	0	2,54	T_{ext}^{19}	0	−0,027	1,44
T_{int}^{6}	−0,016	−0,016	0,64	T_{ext}^{1}	0	−0,027	0,31	T_{ext}^{20}	0,001	0,027	1,61
T_{int}^{7}	−0,016	0,016	0,64	T_{ext}^{2}	0	0,027	0,66	T_{ext}^{21}	0,018	0,020	1,61
T_{int}^{8}	−0,015	0,015	0,64	T_{ext}^{3}	0,019	0,019	0,66	T_{ext}^{22}	0,027	0,004	1,61
T_{int}^{9}	0	0	0,64	T_{ext}^{4}	0,027	0	0,66	T_{ext}^{23}	0,021	−0,017	1,61
T_{int}^{10}	0,016	−0,016	0,64	T_{ext}^{5}	0,019	−0,019	0,66	T_{ext}^{24}	0,004	−0,027	1,61
T_{int}^{11}	0	0,023	1,14	T_{ext}^{6}	−0,002	−0,027	0,66	T_{ext}^{25}	−0,016	−0,022	1,62
T_{int}^{12}	0	0,008	1,14	T_{ext}^{7}	−0,017	−0,021	0,66	T_{ext}^{26}	−0,027	−0,001	1,62
T_{int}^{13}	0	−0,008	1,14	T_{ext}^{8}	−0,027	0	0,66	T_{ext}^{27}	−0,020	0,018	1,62
T_{int}^{14}	0	−0,023	1,14	T_{ext}^{9}	−0,021	0,017	0,66	T_{ext}^{28}	0	−0,027	1,84
T_{int}^{15}	0,016	0,016	1,639	T_{ext}^{10}	0	−0,027	0,84	T_{ext}^{29}	0	−0,027	2,04
T_{int}^{16}	0,006	0,006	1,639	T_{ext}^{11}	0,001	−0,027	1,0394	T_{ext}^{30}	0	−0,027	2,24
T_{int}^{17}	−0,006	−0,006	1,639	T_{ext}^{12}	−0,018	0,020	1,16234	T_{ext}^{31}	0	−0,027	2,4366
T_{int}^{18}	−0,016	−0,016	1,64	T_{ext}^{13}	0,025	0,010	1,15934	T_{ext}^{32}	0	−0,027	2,5366
T_{int}^{19}	−0,016	0,016	1,64	T_{ext}^{14}	0,025	0,009	1,16				

transfer is the fast fluidization, in which there is a phase inversion. There is a relatively dense zone at the bottom of the suspension followed by a dilute zone where clusters or particles are ejected upward [24]. Although the latter regime might be a good compromise for the heat transfer, it is more difficult to control the suspension from a practical point of view, and it needs high air velocities – i.e. high air flow rates – which is finally associated to high power consumption to compressed the air in the case of a commercial-scale power plant. Finally, the best compromise in terms of both heat transfer and energy consumption is the turbulent fluidization regime.

To confirm the previous conclusion, Fig. 14 presents the radial temperatures distribution associated to the three tests presented in Table 4 for particle temperatures of approximately 400 °C, i.e. for three fluidization regimes. In the figures, each color corresponds to a specific height where such profiles can be measured, namely, the three well instrumented sections at the bottom, middle and top of the irradiated zone (cf. Fig. 3). The negative x-axis values correspond to the irradiated face of the tube, and the vertical dashed lines represent the tube thickness. First, the particle temperature inside the tube is very homogenous, whatever the fluidization regime, which highlight the good mixing inherent to fluidized bed. Second, for an increase of the particle temperature nearly equivalent for the three tests, $\Delta T_{part} \approx 400$ °C, the temperature difference between the wall and the particles is the lowest in the turbulent fluidization case. This is coherent with the dimensionless heat transfer index presented in Table 4. Third, due to both the cavity effect and the conduction in the tube thickness, the external temperatures at the back face are always higher than the particle temperatures inside the tube. The previous analysis confirms that the dimensionless heat transfer index is a relevant indicator of the quality of the heat transfer.

4. Conclusion

The thermal performances of a gas-particle dense suspension used as heat transfer fluid in a tubular solar receiver irradiated along 1 m are assessed over a large range of the operating parameters. Olivine particles belonging to Geldart class A are selected as solid medium with mass flux up to 93 mg/(m^{2}s). Incident solar flux density configurations between 220 and 600 suns are tested, with various distribution homogeneity.

The main findings are related to the receiver thermal behavior with respect to the incident solar flux density, particle temperature increase through the receiver tube and the associated thermal efficiency, the dynamic response of the system, the experimental values of the heat transfer coefficient and the link between the heat transfer coefficient and the fluidization regimes.

Even if the recommended operation solar flux density is 400 – 500 kW/m^2, the system can hold high peak densities (from 800 suns at the bottom of the tube to 250 suns only 60 cm above).

The maximum particle temperature increase along the 1 m irradiated length reaches 650 °C for a medium incident solar power of approximately 30 kW and particle preheating to 300 °C in the dispenser. The thermal efficiency varies in the range 40 – 70 % for particle mass flux between 15 and 80 kg/(m^{2}s). The thermal efficiency can be improved using a cavity-type solar receiver.

The dynamic responses of the system are studied, showing that the control of the receiver can be pressure-based or based on the aeration flow rate, for respectively large and small variations of the particle mass flux and temperature. For example, a 10 % increase of the pressure in the dispenser results in a 90 % increase of the particle mass flux, whereas it is only 16 % for a 33 % increase of the aeration flow rate. The duration of the transient phases is relatively small for both types of control, typically 60 – 70 s.

The measured global mean heat transfer coefficient is 1000 ± 200 W/(m^{2}K) for particle mass flux above 15 kg/(m^{2}s), with peak values at 1500 W/(m^{2}K).

A dimensionless heat transfer index is derived. It enables to highlights (i) the increase of the heat transfer with the temperature, and (ii) the influence of the fluidization regime on the heat transfer intensity. The turbulent fluidization regime corresponds to the highest heat transfer index.

Declaration of Competing Interest

The authors declare that they have no known competing financial interests or personal relationships that could have appeared to influence the work reported in this paper.

Acknowledgements

The characterization of the olivine sample was conducted with the help of the Material Characterization Platform – Surfaces and Interfaces Analyses of the PROMES (CNRS) laboratory. Special thanks to Regis Rodriguez for his help with the Labview acquisition software.

Funding.

This work was funded by the French "Investments for the future" ("*Investissements d'Avenir*") program managed by the National Agency for Research (ANR) under contract ANR-10-LABX-22-01 (Labex SOLSTICE).

Appendix A. Instrumentation of the Set-Up

Tables A1 and A2 list respectively the position of the pressure probes and of the thermocouples in the main tube, in Cartesian coordinates, where the origin {0 0 0} is the center of the tube at the height of the aeration injection.

Appendix B. Uncertainties on the heat transfer coefficient

The uncertainty on the heat transfer coefficient, $\delta h_{wall,part}$, is given by Equation (13). In this equation, $\delta(\Delta T_{wall,part})$ is the uncertainty of the logarithmic mean of the temperatures differences between the internal wall and the particles. It is determined by Equations (14)–(16) by using the method of the differentials. To simplify the reading of the equations, $\Delta T^{in,out} = T^{in,out}_{wall,int} - T^{in,out}_{part}$, and thus the associated uncertainties $\delta(\Delta T^{in,out}) = \delta T^{in,out}_{paroi,int} + \delta T^{in,out}_{part}$.

$$\frac{\delta h_{wall,part}}{h_{wall,part}} = \frac{\delta \phi_{abs}}{\phi_{abs}} + \frac{\delta S_{exch}}{S_{exch}} + \frac{\delta(\Delta T_{wall,part})}{\Delta T_{wall,part}} \tag{13}$$

$$\delta(\Delta T_{wall,part}) = \left|\frac{\partial(\Delta T_{wall,part})}{\partial(\Delta T^{in})}\right| \delta(\Delta T^{in}) + \left|\frac{\partial(\Delta T_{wall,part})}{\partial(\Delta T^{out})}\right| \delta(\Delta T^{out}) \tag{14}$$

$$\frac{\partial(\Delta T_{wall,part})}{\partial(\Delta T^{in})} = \frac{\ln\left(\frac{\Delta T^{in}}{\Delta T^{out}}\right) - \frac{\Delta T^{in} - \Delta T^{out}}{\Delta T^{in}}}{\left(\ln\left(\frac{\Delta T^{in}}{\Delta T^{out}}\right)\right)^2} \tag{15}$$

$$\frac{\partial(\Delta T_{wall,part})}{\partial(\Delta T^{out})} = \frac{-\ln\left(\frac{\Delta T^{in}}{\Delta T^{out}}\right) + \frac{\Delta T^{in} - \Delta T^{out}}{\Delta T^{out}}}{\left(\ln\left(\frac{\Delta T^{in}}{\Delta T^{out}}\right)\right)^2} \tag{16}$$

Appendix C. Supplementary data

Supplementary data to this article can be found online at https://doi.org/10.1016/j.solener.2023.112118.

References

[1] Alloy Wire International, Inconel 601 [WWW Document], 2020. URL www.alloywire.fr/products/inconel-601 (accessed 9.11.20).
[2] M.V. Bagepalli, S.Y. Jeong, J.D. Brooks, Z.M. Zhang, D. Ranjan, P.G. Loutzenhiser, Experimental characterization of extreme temperature granular flows for solar thermal energy transport and storage, Sol. Energy Mater. Sol. Cells 248 (2022), 112020, https://doi.org/10.1016/j.solmat.2022.112020.
[3] M. Balat-Pichelin, J.-L. Sans, E. Bêche, L. Charpentier, A. Ferrière, S. Chomette, Emissivity at high temperature of Ni-based superalloys for the design of solar receivers for future tower power plants, Sol. Energy Mater. Sol. Cells 227 (2021), 111066, https://doi.org/10.1016/j.solmat.2021.111066.
[4] M. Bartels, W. Lin, J. Nijenhuis, F. Kapteijn, J.R. van Ommen, Agglomeration in fluidized beds at high temperatures: Mechanisms, detection and prevention, Prog. Energy Combust. Sci. 34 (2008) 633–666, https://doi.org/10.1016/j.pecs.2008.04.002.
[5] O. Behar, B. Grange, G. Flamant, Design and performance of a modular combined cycle solar power plant using the fluidized particle solar receiver technology, Energ. Conver. Manage. 220 (2020), 113108, https://doi.org/10.1016/j.enconman.2020.113108.
[6] H. Benoit, R. Ansart, H. Neau, P. Garcia Triñanes, G. Flamant, O. Simonin, Three-dimensional numerical simulation of upflow bubbling fluidized bed in opaque tube under high flux solar heating, AIChE J 64 (2018) 3857–3867, https://doi.org/10.1002/aic.16218.
[7] H. Benoit, I. Pérez López, D. Gauthier, J.-L. Sans, G. Flamant, On-sun demonstration of a 750 °C heat transfer fluid for concentrating solar systems: Dense particle suspension in tube, Sol. Energy 118 (2015) 622–633, https://doi.org/10.1016/j.solener.2015.06.007.
[8] H. Benoit, L. Spreafico, D. Gauthier, G. Flamant, Review of heat transfer fluids in tube-receivers used in concentrating solar thermal systems: Properties and heat transfer coefficients, Renew. Sustain. Energy Rev. 55 (2016) 298–315, https://doi.org/10.1016/j.rser.2015.10.059.
[9] H.T. Bi, N. Ellis, I.A. Abba, J.R. Grace, A state-of-the-art review of gas–solid turbulent fluidization, Chem. Eng. Sci. 55 (2000) 4789–4825, https://doi.org/10.1016/S0009-2509(00)00107-X.
[10] B. Boissiere, R. Ansart, D. Gauthier, G. Flamant, M. Hemati, Experimental hydrodynamic study of gas-particle dense suspension upward flow for application as new heat transfer and storage fluid, Can. J. Chem. Eng. 93 (2015) 317–330, https://doi.org/10.1002/cjce.22087.
[11] M. Castro-Quijada, D. Faundez, R. Rojas, A. Videla, Improving the working fluid based on a NaNO3-KNO3-NaCl-KCl molten salt mixture for concentrating solar power energy storage, Sol. Energy 231 (2022) 464–472, https://doi.org/10.1016/j.solener.2021.11.058.
[12] CSP2 Project: Dense Suspensions of Solid Particles as a New Heat Transfer Fluid for CSP [WWW Document], 2015. URL https://cordis.europa.eu/project/id/282932 (accessed 12.12.22).

[13] H. Cui, P. Sauriol, J. Chaouki, High temperature fluidized bed reactor: measurements, hydrodynamics and simulation, Chem. Eng. Sci. 58 (2003) 1071–1077, https://doi.org/10.1016/S0009-2509(02)00649-8.
[14] Y. Deng, F. Sabatier, R. Dewil, G. Flamant, A. Le Gal, R. Gueguen, J. Baeyens, S. Li, R. Ansart, Dense upflow fluidized bed (DUFB) solar receivers of high aspect ratio: Different fluidization modes through inserting bubble rupture promoters, Chem. Eng. J. 418 (2021), 129376, https://doi.org/10.1016/j.cej.2021.129376.
[15] M.T. Dunham, B.D. Iverson, High-efficiency thermodynamic power cycles for concentrated solar power systems, Renew. Sustain. Energy Rev. 30 (2014) 758–770, https://doi.org/10.1016/j.rser.2013.11.010.
[16] M. Ebert, L. Amsbeck, J. Rheinländer, B. Schlögl-Knothe, S. Schmitz, M. Sibum, R. Uhlig, R. Buck, Operational experience of a centrifugal particle receiver prototype, in: Presented at the SOLARPACES 2018: International Conference on Concentrating Solar Power and Chemical Energy Systems, 2019, p. 030018, https://doi.org/10.1063/1.5117530.
[17] G. Flamant, D. Gauthier, H. Benoit, J.-L. Sans, R. Garcia, B. Boissière, R. Ansart, M. Hemati, Dense suspension of solid particles as a new heat transfer fluid for concentrated solar thermal plants: On-sun proof of concept, Chem. Eng. Sci. 102 (2013) 567–576, https://doi.org/10.1016/j.ces.2013.08.051.
[18] G. Flamant, B. Grange, J. Wheeldon, F. Siros, B. Valentin, F. Bataille, H. Zhang, Y. Deng, J. Baeyens, Opportunities and challenges in using particle circulation loops for concentrated solar power applications, Prog. Energy Combust. Sci. 94 (2023), 101056, https://doi.org/10.1016/j.pecs.2022.101056.
[19] G. Flamant, M. Hemati, Dispositif Collecteur D'energie Solaire. (2010), 1058565.
[20] R. Flesch, H. Stadler, R. Uhlig, R. Pitz-Paal, Numerical analysis of the influence of inclination angle and wind on the heat losses of cavity receivers for solar thermal power towers, Sol. Energy 110 (2014) 427–437, https://doi.org/10.1016/j.solener.2014.09.045.
[21] B. Formisani, R. Girimonte, L. Mancuso, Analysis of the fluidization process of particle beds at high temperature, Chem. Eng. Sci. 53 (1998) 951–961, https://doi.org/10.1016/S0009-2509(97)00370-9.
[22] D. Geldart, Chap. 6: Particle Entrainment and Carryover, in: Gas Fluidization Technology. John Wiley & Sons Ltd.: Chichester, U.K., 1986. pp. 123–154.
[23] D. Geldart, Types of gas fluidization, Powder Technol. 7 (1973) 285–292, https://doi.org/10.1016/0032-5910(73)80037-3.
[24] J.R. Grace, X. Bi, N. Ellis, Chap. 9: Turbulent Fluidization, in: Essential of Fluidization Technology. John Wiley & Sons Ltd.: Chichester, U.K., 2020a. pp. 163–180.
[25] J.R. Grace, X. Bi, N. Ellis Chap. 14: Heat and Mass Transfer, in: Essential of Fluidization Technology. John Wiley & Sons Ltd.: Chichester, U.K., 2020b. pp. 291–332.
[26] R. Gueguen, B. Grange, F. Bataille, S. Mer, G. Flamant, Shaping High Efficiency, High Temperature Cavity Tubular Solar Central Receivers, Energies 13 (2020) 4803, https://doi.org/10.3390/en13184803.
[27] R. Gueguen, S. Mer, A. Toutant, F. Bataille, G. Flamant, Effect of temperature on the hydrodynamics of a fluidized bed circulating in a long tube for a solar energy harvesting application, Chem. Eng. Sci. (2023), 119218, https://doi.org/10.1016/j.ces.2023.119218.
[28] R. Gueguen, G. Sahuquet, S. Mer, A. Toutant, F. Bataille, G. Flamant, Fluidization Regimes of Dense Suspensions of Geldart Group A Fluidized Particles in a High Aspect Ratio Column, Chem. Eng. Sci. (2022), 118360, https://doi.org/10.1016/j.ces.2022.118360.
[29] R. Gueguen, G. Sahuquet, S. Mer, A. Toutant, F. Bataille, G. Flamant, Gas-Solid Flow in a Fluidized-Particle Tubular Solar Receiver: Off-Sun Experimental Flow Regimes Characterization, Energies 14 (2021) 7392, https://doi.org/10.3390/en14217392.
[30] E. Guillot, R. Rodriguez, N. Boullet, J.-L. Sans, ARGOS: Solar furnaces flat heliostats tracking error estimation with a direct camera-based vision system. Presented at the SolarPACES 2017: International Conference on Concentrating Solar Power and Chemical Energy Systems, Santiago, Chile, p. 200001. 2018. 10.1063/1.5067202.
[31] C.K. Ho, A review of high-temperature particle receivers for concentrating solar power, Appl. Therm. Eng. 109 (2016) 958–969, https://doi.org/10.1016/j.applthermaleng.2016.04.103.
[32] Ho, C.K., Christian, J., Yellowhair, J., Jeter, S., Golob, M., Nguyen, C., Repole, K., Abdel-Khalik, S., Siegel, N., Al-Ansary, H., El-Leathy, A., Gobereit, B., 2017. Highlights of the high-temperature falling particle receiver project: 2012 - 2016. Presented at the SOLARPACES 2016: International Conference on Concentrating Solar Power and Chemical Energy Systems, Abu Dhabi, United Arab Emirates, p. 030027. 10.1063/1.4984370.
[33] C.K. Ho, A.R. Mahoney, A. Ambrosini, M. Bencomo, A. Hall, T.N. Lambert, Characterization of Pyromark 2500 Paint for High-Temperature Solar Receivers, J. Sol. Energy Eng. 136 (2014), 014502, https://doi.org/10.1115/1.4024031.
[34] K. Jiang, X. Du, Q. Zhang, Y. Kong, C. Xu, X. Ju, Review on gas-solid fluidized bed particle solar receivers applied in concentrated solar applications: Materials, configurations and methodologies, Renew. Sustain. Energy Rev. 150 (2021), 111479, https://doi.org/10.1016/j.rser.2021.111479.
[35] Q. Kang, G. Flamant, R. Dewil, J. Baeyens, H.L. Zhang, Y.M. Deng, Particles in a circulation loop for solar energy capture and storage, Particuology 43 (2019) 149–156, https://doi.org/10.1016/j.partic.2018.01.009.
[36] D. Kunii, O. Levenspiel, Chap. 3: Fluidization and Mapping of Regimes, in: Fluidization Engineering, Elsevier, 1991, pp. 61–94, https://doi.org/10.1016/B978-0-08-050664-7.50009-3.
[37] Laubscher, H.F., Albrecht, K.J., Ho, C.K., 2020. High-Temperature Particle Flow Testing in Parallel Plates for Particle-to-Supercritical CO2 Heat Exchanger Applications, in: ASME 2020 14th International Conference on Energy Sustainability. Presented at the ASME 2020 14th International Conference on Energy Sustainability, American Society of Mechanical Engineers, Virtual, Online, p. V001T02A011. 10.1115/ES2020-1664.
[38] A. Le Gal, B. Grange, M. Tessonneaud, A. Perez, C. Escape, J.-L. Sans, G. Flamant, Thermal analysis of fluidized particle flows in a finned tube solar receiver, Sol. Energy 191 (2019) 19–33, https://doi.org/10.1016/j.solener.2019.08.062.
[39] B. Leckner, Regimes of large-scale fluidized beds for solid fuel conversion, Powder Technol. 308 (2017) 362–367, https://doi.org/10.1016/j.powtec.2016.11.070.
[40] S. Leimbach, J. Lukas, S. Kolb, L. Yang, T. Plankenbühler, M. Sega, J. Harting, J. Karl, Early Detection of Agglomeration in Fluidized Beds by Means of Frequency Analysis of Pressure Fluctuations, Energy Fuels 36 (2022) 4924–4932, https://doi.org/10.1021/acs.energyfuels.1c04356.
[41] MCI Technologies, Properties of Insulfrax [WWW Document], 2020. URL https://www.mci-tech.com/produits/nappes-et-feutres-ht/insulfrax (accessed 9.11.20).
[42] Next-CSP Project: High Temperature Concentrated Solar Thermal Plant with Particle Receiver and Direct Thermal Storage [WWW Document], 2020. URL https://cordis.europa.eu/project/id/727762 (accessed 12.12.22).
[43] I. Perez Lopez, H. Benoit, D. Gauthier, J.L. Sans, E. Guillot, G. Mazza, G. Flamant, On-sun operation of a 150 kWth pilot solar receiver using dense particle suspension as heat transfer fluid, Sol. Energy 137 (2016) 463–476, https://doi.org/10.1016/j.solener.2016.08.034.
[44] E. Rabinovich, H. Kalman, Flow regime diagram for vertical pneumatic conveying and fluidized bed systems, Powder Technol. 207 (2011) 119–133, https://doi.org/10.1016/j.powtec.2010.10.017.
[45] A. Reyes Urrutia, H. Benoit, M. Zambon, D. Gauthier, G. Flamant, G. Mazza, Simulation of the behavior of a dense SiC particle suspension as an energy transporting vector using computational fluid dynamics (CFD), Chem. Eng. Res. Des. 106 (2016) 141–154, https://doi.org/10.1016/j.cherd.2015.12.008.
[46] A. Salomé, F. Chhel, G. Flamant, A. Ferrière, F. Thiery, Control of the flux distribution on a solar tower receiver using an optimized aiming point strategy: Application to THEMIS solar tower, Sol. Energy 94 (2013) 352–366, https://doi.org/10.1016/j.solener.2013.02.025.
[47] F. Trombe, A. Le Phat Vinh, Thousand kW solar furnace, built by the National Center of Scientific Research, in Odeillo (France), Sol. Energy 15 (1973) 57–61, https://doi.org/10.1016/0038-092X(73)90006-6.
[48] W. Wu, L. Amsbeck, R. Buck, R. Uhlig, R. Ritz-Paal, Proof of Concept Test of a Centrifugal Particle Receiver, Energy Procedia 49 (2014) 560–568, https://doi.org/10.1016/j.egypro.2014.03.060.
[49] J. Yerushalmi, N.T. Cankurt, Further studies of the regimes of fluidization, Powder Technol. 24 (1979) 187–205, https://doi.org/10.1016/0032-5910(79)87036-9.
[50] H. Zhang, W. Kong, T. Tan, F. Gilles, J. Baeyens, Experiments support an improved model for particle transport in fluidized beds, Sci. Rep. 7 (2017) 10178, https://doi.org/10.1038/s41598-017-10597-3.